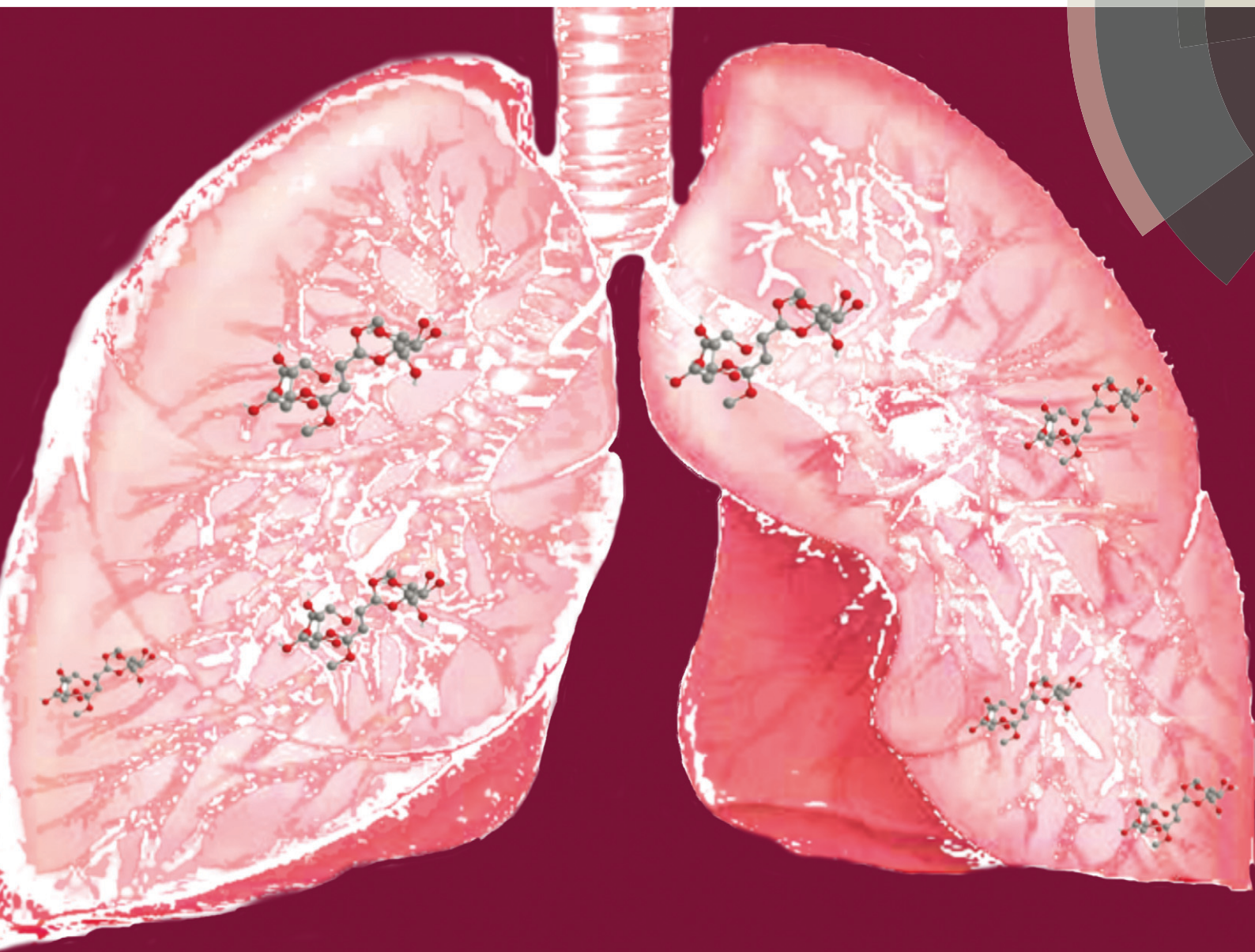


# Molecular Systems Design & Engineering

Building and designing systems from the molecular level

<http://rsc.li/molecular-engineering>



ISSN 2058-9689



**PAPER**

Heidi M. Mansour *et al.*

Microparticulate/nanoparticulate powders of a novel Nrf2 activator and an aerosol performance enhancer for pulmonary delivery targeting the lung Nrf2/Keap-1 pathway

**IChemE** ADVANCING  
CHEMICAL  
ENGINEERING  
WORLDWIDE



Cite this: *Mol. Syst. Des. Eng.*, 2016, 1, 48

## Microparticulate/nanoparticulate powders of a novel Nrf2 activator and an aerosol performance enhancer for pulmonary delivery targeting the lung Nrf2/Keap-1 pathway

Priya Muralidharan,<sup>a</sup> Don Hayes Jr.,<sup>bc</sup> Stephen M. Black<sup>d</sup> and Heidi M. Mansour<sup>\*aefg</sup>

This systematic and comprehensive study reports for the first time on the successful rational design of advanced inhalable therapeutic dry powders containing dimethyl fumarate, a first-in-class Nrf2 activator drug to treat pulmonary inflammation, using particle engineering design technology for targeted delivery to the lungs as advanced spray dried (SD) one-component DPIs. In addition, two-component co-spray dried (co-SD) DMF :  $\alpha$ -Man DPIs with high drug loading were successfully designed for targeted lung delivery as advanced DPIs using organic solution advanced spray drying in closed mode. Regional targeted deposition using design of experiments (DoE) for *in vitro* predictive lung modeling based on aerodynamic properties was tailored based on composition and spray drying parameters. These findings indicate the significant potential of using  $\alpha$ -Man in spray drying to improve particle formation and aerosol performance of small molecule with a relatively low melting point. These respirable microparticles/nanoparticles in the solid-state exhibited excellent aerosol dispersion performance with an FDA-approved human DPI device. Using *in vitro* predictive lung deposition modeling, the aerosol deposition patterns of these particles show the capability to reach lower airways to treat inflammation in this region in pulmonary diseases such as acute lung injury (ALI), chronic obstructive pulmonary disease (COPD), pulmonary hypertension (PH), and pulmonary endothelial disease.

Received 5th November 2015,  
Accepted 4th January 2016

DOI: 10.1039/c5me00004a

rsc.li/molecular-engineering

## Introduction

Acute lung injury (ALI) and the acute respiratory distress syndrome (ARDS) are life-threatening conditions that occur in critically ill patients, including patients who experience shock, trauma, sepsis, burns, aspiration, or pneumonia. Although the terms ALI and ARDS are often used interchangeably, strict criteria reserve ARDS for the most severe form of the disease. Clinical manifestations include inflammatory responses of the lung to both direct and indirect insults and

are characterized by severe hypoxemia, hypercapnia, diffuse infiltration on radiographs, and a substantial reduction in pulmonary compliance. Although mechanical ventilation (MV) is crucial for maintaining life during ALI/ARDS, the mechanical forces generated during ventilation can further damage the lungs due to alveolar distension, barotrauma, and cyclic airway closing and reopening. This phenomenon, ventilator associated lung injury (VALI), can trigger a pulmonary and systemic inflammatory reaction leading to multiple organ dysfunction and organ failure.

Chronic obstructive pulmonary disease (COPD) is a chronic disease occurring primarily in elderly patients that is often associated with chronic inflammatory response leading to airflow limitation. The pathophysiology of COPD<sup>1</sup> involves chronic inflammation of the airways due to chronic bronchitis and emphysema. Alveolar macrophages play a key role in this inflammatory response by releasing inflammatory mediators including tumor necrosis factor- $\alpha$  (TNF- $\alpha$ ), interleukin (IL)-6, IL-8, monocyte chemotactic peptide (MCP)-1, leukotriene LTB4 and reactive oxygen species (ROS).<sup>2</sup> In patients with COPD, cellular remodeling of airway smooth muscle occurs more often and this is not fully reversible. Current, treatment options for COPD includes anticholinergics, beta<sub>2</sub>-agonists,

<sup>a</sup> College of Pharmacy, Skaggs Pharmaceutical Sciences Center, The University of Arizona, 1703 E. Mabel St, Tucson, AZ 85721-0202, USA.

E-mail: mansour@pharmacy.arizona.edu; Tel: +1 520 626 2768

<sup>b</sup> Departments of Pediatrics and Internal Medicine, Lung and Heart-Lung Transplant Programs, The Ohio State University College of Medicine, Columbus, OH 43205, USA

<sup>c</sup> The Davis Heart and Lung Research Institute, The Ohio State University College of Medicine, Columbus, OH 43205, USA

<sup>d</sup> Department of Medicine, Division of Translational and Regenerative Medicine, The University of Arizona, Tucson, AZ, 85724, USA

<sup>e</sup> Institute of the Environment, The University of Arizona, Tucson, AZ 85721, USA

<sup>f</sup> National Cancer Institute Comprehensive Cancer Center, The University of Arizona, Tucson, AZ 85721, USA

<sup>g</sup> The BIO5 Research Institute, The University of Arizona, Tucson, AZ 85721, USA



and inhaled corticosteroids.<sup>3–5</sup> Current therapeutics control the symptoms but do not cure the underlying disease.<sup>6</sup> Similarly, in disease such as pulmonary hypertension (PH) there is both pulmonary endothelial injury and remodeling of the pulmonary smooth muscle layer. Based upon a large number of studies in animal models, the three major stimuli that drive the vascular remodeling process are shear stress,<sup>7,8</sup> inflammation,<sup>9,10</sup> and hypoxia.<sup>11</sup> Although, the precise mechanisms by which these stimuli impair pulmonary vascular function increased oxidative stress is thought to play a major role is unresolved. The oxidative stress in PH has been linked to increases in uncoupled endothelial nitric oxide synthase (eNOS),<sup>12</sup> increases in the activity of xanthine oxidase<sup>13</sup> and NADPH oxidase<sup>14</sup> activity as well as mitochondrial dysfunction.<sup>15</sup>

Dimethyl fumarate (DMF), is shown to possess anti-inflammatory<sup>16</sup> property that can be explored to target the cellular inflammatory response pathway<sup>6</sup> and protect against oxidative stress in patients with COPD.<sup>17</sup> DMF is a fumaric acid ester known for its therapeutic activity in treating multiple sclerosis (MS) and psoriasis. Its efficiency in treating psoriasis vulgaris was introduced through self-experiment by German chemist Walter Schweckendieck.<sup>18</sup> Several years later, DMF was approved for topical skin administration as Fumaderm® for treating dermatologic conditions in Europe. Recently, the DMF was approved in the United States as an orally administered delayed-release capsule, Tecfidera® (Biogen, Research Triangle Park, NC) to treat the autoimmune neurological disease, multiple sclerosis. The approval of DMF to treat multiple sclerosis has opened doors to new avenues for research in using DMF in other inflammatory and autoimmune conditions, such as polyarthritis, vascular calcification,<sup>19</sup> renal fibrosis,<sup>20</sup> and pancreatitis.<sup>21,22</sup>

It has been shown that DMF possess both anti-inflammatory and anti-oxidant properties. Its mode of action as an anti-oxidant is attributed to its ability to activate the nuclear factor (erythroid – derived 2) – like 2 (Nrf2) genetic pathway and so reduce oxidative stress.<sup>23,24</sup> In normal cells, Nrf2 is sequestered by the Kelch like – ECH-associated protein 1 (Keap-1) to form a Nrf2–Keap 1 complex. However, during oxidative stress Nrf2 dissociates from Keap-1, translocates into the nucleus and binds to electrophile response elements (ARE), promoting the transcription of the target gene. DMF activates the dissociation of Nrf2 from Keap-1 by selectively blocking, or binding to, reactive cysteine residues in Keap-1.<sup>19</sup>

Nrf2 has been reported to alleviate lung inflammation following lung injury<sup>25</sup> and its anti-inflammatory property is attributed to its ability to prevent nuclear factor kappa B (NF-κB) translocation into the nucleus.<sup>26</sup> As a result, NF-κB dependent gene expression is attenuated. Siedel *et al.*, have shown that in the airway, DMF exhibits both an anti-inflammatory effect, by inhibiting NF-κB<sup>6</sup> and an ability to attenuate airway smooth muscle cell proliferation through induction of heme-oxygenase-1 (HO-1).<sup>27</sup> There is increasing interest in exploring the anti-oxidant signaling pathway (Nrf2), for anti-inflammatory therapy and stimulating the Nrf2 pathway in alveolar

macrophages has been shown to prevent the exacerbation of COPD caused by bacterial infection.<sup>28</sup>

Little is known regarding the role of Nrf2 in pulmonary endothelial diseases such as PH. However, it has been shown that Nrf2 is stimulated in endothelial cells, exposed to laminar shear stress.<sup>29</sup> Increased shear stress is thought to be a major component of the endothelial dysfunction associated with certain congenital heart defects that result in increased pulmonary blood flow.<sup>7,8</sup> Interestingly, oscillatory shear stress, such as that observed during the development of atherosclerosis and which results in reduced NO (nitric oxide) production and increased superoxide generation<sup>30</sup> decreases Nrf2-mediated activation of ARE-linked genes and transitions the endothelium to a proathrogenic state.<sup>31</sup> Recent evidence also suggests that the Nrf2–Keap1 complex may be tethered to the mitochondrion and this complex may directly sense ROS that are released from mitochondria.<sup>32</sup> As mitochondrial ROS are stimulated during the development of endothelial dysfunction<sup>33–35</sup> this may allow Nrf2 signaling to be stimulated. A potential concern in using Nrf2 activators in a non-targeted manner is the reported dual role of the Nrf2 pathway in cancer progression, as reported by Zhang *et al.*<sup>36</sup> To overcome this deleterious action we propose a targeted delivery to the lungs, using inhalation delivery, which would target the Nrf2 activators to the intended site of action in the organ and significantly reduce, or even eliminate, off-target side effects.

Hence, in this systematic and comprehensive study, we have engineered DMF into advanced inhalable dry powders that can be targeted to the respiratory tract as dry powder inhalers (DPIs) using an FDA-approved human DPI device. Organic solution closed mode advanced spray drying was employed to exploit the unique advantages of organic solvents over aqueous in forming dry particles that are both inhalable and high performing as DPIs, as we have reported.<sup>37–41</sup> There is of plethora of literature on the various types of nanomaterials that can be used in drug delivery.<sup>42–45</sup> In addition to advanced spray drying under rationally chosen spray drying conditions to engineer spray dried (SD) DMF nanostructured inhalable powders, DMF was co-spray dried (co-SD) with D-mannitol (D-Man) at various molar ratios with high drug loading. D-Man is a non-reducing sugar, a mucolytic agent, and an aerosol performance enhancer in DPIs. We chose D-Man based on our previously study in which D-Man significantly improved *in vitro* aerosol dispersion performance.<sup>46</sup> To the authors' knowledge, we are the first to report on inhalable microparticles/nanoparticles of DMF and co-SD DMF:D-Man for targeted pulmonary delivery as advanced DPIs.

## Experimental: materials and methods

### Materials

DMF [97% purity] [C<sub>6</sub>H<sub>8</sub>O<sub>4</sub>; molecular weight (MW): 144.12 g mol<sup>–1</sup>], shown in Fig. 1 (ChemDraw Ultra Ver. 10.0.; CambridgeSoft, Cambridge, Massachusetts), was obtained from Sigma-Aldrich (St. Louis, Missouri). Raw Man (C<sub>6</sub>H<sub>14</sub>O<sub>6</sub>;





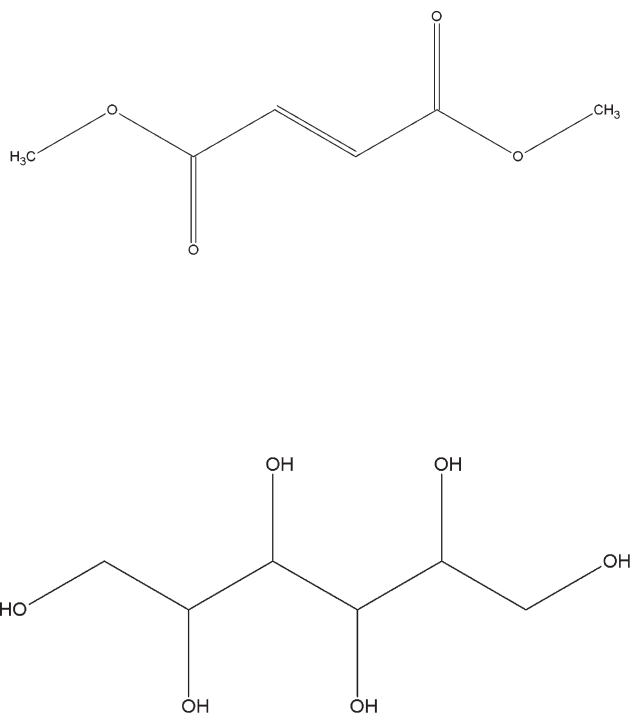


Fig. 1 Chemical structures of DMF (top) and D-mannitol (bottom).

MW: 182.17 g mol<sup>-1</sup>) (Fig. 1) was obtained from Acros Organics (New Jersey, USA). Methanol (HPLC grade, ACS-certified grade, purity 99.9%) was obtained from Fisher Scientific (Fair Lawn, New Jersey). HYDRANAL®-Coulomat AD was obtained from Sigma-Aldrich. The nitrogen gas used was ultra-high purity (UHP) nitrogen gas (Cryogenics and gas facility, The University of Arizona, Tucson, Arizona). Raw DMF was stored in sealed glass desiccators over Indicating Drierite/Drierite™ desiccant at room temperature. Raw D-Man was used as received and stored under room conditions. Other chemicals were stored under room conditions.

## Methods

**Preparation of SD and co-SD particles by organic solution advanced spray drying in closed mode.** Organic solution advanced spray drying process in the absence of water was performed in closed mode using a Büchi B-290 Mini Spray Dryer with a high performance cyclone in closed mode using UHP dry nitrogen gas as the atomizing drying gas and connected to the B-295 Inert Loop (Büchi Labortechnik AG, Flawil, Switzerland). The feed solution was prepared by dissolving the component/s in methanol using Branson 7500 ultrasonicator to aid in dissolution. For the two-component system, the components were dissolved successively in the solvent consisting of drug with Man in rationally selected molar ratios in methanol. Table 1 lists the spray drying conditions for one- and two-component powders. The drying gas atomization rate (670 L h<sup>-1</sup> at 55 mm in height) and aspiration rate (35 m<sup>3</sup> h<sup>-1</sup> at 100% rate) was maintained constant during all the experiments. Three feed pump rates were employed to obtain particles using pump rates of 7.5 mL min<sup>-1</sup> (low, 25%), 15 mL min<sup>-1</sup> (medium, 50%), and 30 mL min<sup>-1</sup> (high, 100%). The stainless steel two-fluid nozzle tip diameter was 0.7 mm with 1.5 mm gas cap. The SD and co-SD particles were separated from the nitrogen drying gas in the high-performance cyclone (HPC) and collected in the small sample collector. All SD and co-SD powders were carefully stored in sealed glass vials stored in sealed glass desiccators over indicating Drierite/Drierite™ desiccant at -20 °C under ambient pressure. For comparison purpose, Man was sprayed as single component under the same conditions as co-SD DMF : Man mixtures.

**Scanning electron microscopy (SEM).** Using conditions similar to previously reported,<sup>38,39,46,47</sup> visual imaging and analysis of particle size, morphology, and surface morphology was achieved by scanning electron microscopy (SEM). The powder samples were placed on double coated carbon conductive adhesive Pelco tabs™ (TedPella, Inc. Redding CA), which were adhered to aluminum stubs (Ted-Pella, Inc.)

**Table 1** Advanced spray drying parameters for spray dried (SD) and co-spray dried (co-SD) powders from methanol (MeOH) solution using organic solution advanced closed mode spray drying particle engineering design

Powder composition (molar ratio)	Molar ratio composition (DMF : D-Man)	Feed concentration in MeOH (% w/v)	Pump rate (%)	Inlet T (°C)	Outlet T (°C)
SD DMF	100 : 0	1	High (100%)	89	30–44
SD DMF	100 : 0	1	Med (50%)	90	38–41 <sup>a</sup>
SD DMF	100 : 0	1	Low (25%)	89–90	46–49 <sup>a</sup>
co-SD DMF : D-MAN	90 : 10	0.81	Low (25%)	90	48–49
co-SD DMF : D-MAN	90 : 10	0.81	Med (50%)	90	37–39
co-SD DMF : D-MAN	90 : 10	0.81	High (100%)	90	19–30
co-SD DMF : D-MAN	80 : 20	0.46	Low (25%)	90	48–49
co-SD DMF : D-MAN	80 : 20	0.46	Med (50%)	90	36–40
co-SD DMF : D-MAN	80 : 20	0.46	High (100%)	90–91	14–24
co-SD DMF : D-MAN	50 : 50	0.18	Low (25%)	89–90	45–50
co-SD DMF : D-MAN	50 : 50	0.18	Med (50%)	90	30–35
co-SD DMF : D-MAN	50 : 50	0.18	High (100%)	90	35–39
SD D-MAN	0 : 100	0.1	Low (25%)	90–91	47–48
SD D-MAN	0 : 100	0.1	Med (50%)	90	31–33
SD D-MAN	0 : 100	0.1	High (100%)	89–90	28–10

<sup>a</sup> No particles obtained.





Subsequently, the powder sample in the stub was sputter coated with thin film of gold using Anatech Hummer 6.2 (Union city, CA, USA) system at 20  $\mu\text{A}$  for 90 s under argon plasma. The electron beam with an accelerating voltage of 30 kV was used at a working distance of 10–10.4 mm. SEM images were captured by SEM FEI Inspect S (Brno, Czech republic) at several magnification levels.

**Particle sizing and size distribution using SEM micrographs.** The mean size, standard deviation and size range of the particles were determined digitally using SigmaScan Pro 5.0.0 (Systat, San Jose, CA, USA), using similar conditions that have been previously reported.<sup>48</sup> Representative micrographs for each particle sample at 15 000 $\times$  magnification was analyzed by measuring the diameter of at least 100 particles per sample.

**X-Ray powder diffraction (XRPD).** Using conditions similar to previously reported,<sup>38,39,46,47</sup> X-ray powder diffraction (XRPD) patterns of samples were collected at room temperature with a PanAnalytical X'pert diffractometer (PANalytical Inc., Westborough, MA, USA) with Cu K $\alpha$  radiation (45 kV, 40 mA, and  $\lambda = 1.5406 \text{ \AA}$ ) between  $5.0^\circ$  and  $70.0^\circ$  ( $2\theta$ ) with a scan rate of  $2.00^\circ$  per minute at ambient temperature. The powder samples were loaded on zero background silicon wafer sample holder and diffraction measured with an X'celerator detector.

**Differential scanning calorimetry (DSC).** Using conditions similar to previously reported,<sup>38,39,46,47</sup> thermal analysis and phase transition measurements were performed on a TA Q1000 differential scanning calorimeter (DSC) (TA Instruments, New Castle, Delaware) equipped with T-Zero® technology, RSC90 automated cooling system, auto sampler and calibrated with indium. Approximately 1–10 mg sample was placed into an anodized aluminum hermetic DSC pan. The T-Zero® DSC pans were hermetically sealed with the T-Zero hermetic press (TA Instruments). An empty hermetically sealed aluminum pan was used as reference pan for all the experiments. UHP nitrogen was used as the purging gas at a rate of 40 mL  $\text{min}^{-1}$ . The samples were heated from  $0.00^\circ\text{C}$  to  $250.00^\circ\text{C}$  at a scanning rate of  $5.00^\circ\text{C min}^{-1}$ . All measurements were carried out in triplicate ( $n = 3$ ).

**Hot stage microscopy (HSM) under cross-polarizers.** Using conditions similar to previously reported,<sup>38,39,46,47</sup> hot-stage microscopy (HSM) studies used a Leica DMLP cross-polarized microscope (Wetzlar, Germany) equipped with a Mettler FP 80 central processor heating unit and Mettler FP82 hot stage (Columbus, OH, USA). Samples were mounted on glass slide and heated from  $25.0^\circ\text{C}$  to  $200.0^\circ\text{C}$  at a heating rate of  $5.00^\circ\text{C min}^{-1}$ . The images were digitally captured using a Nikon coolpix 8800 digital camera (Nikon, Tokyo, Japan) under  $10\times$  optical objective and  $10\times$  digital zoom.

**Karl Fisher titration (KFT).** Using conditions similar to previously reported,<sup>38,39,46,47</sup> the residual water content of all SD and co-SD powders were quantified analytically by Karl Fischer titration (KFT) coulometrically using a TitroLine 7500 trace titrator (SI Analytics, Germany). Approximately 5–20 mg of powder was added to the titration cell containing Hydranal®Coulomat AD reagent. The residual water content was then calculated.

**Confocal Raman microspectroscopy (CRM), chemical imaging, and mapping.** Confocal Raman microspectroscopy (CRM) provides noninvasive and nondestructive microspectroscopic component analysis of DPI formulations. Using similar conditions previously reported,<sup>38,39,46,47</sup> Raman spectra was obtained at 514 nm laser excitation using Renishaw InVia Reflex (Gloucestershire, UK) at the surface using a  $20\times$  magnification objective on a Leica DM2700 optical microscope (Wetzlar, Germany) and equipped with a Renishaw inVia Raman system (Gloucestershire, UK). This Renishaw system has a  $2400 \text{ l mm}^{-1}$  grating, with a slit width of  $65 \mu\text{m}$  and a thermoelectrically cooled Master Renishaw CCD detector. The laser power was adjusted to achieve 5000 counts per second for the  $520 \text{ cm}^{-1}$  line of the internal Si reference. Raman spectral map was obtained with the stage moved in increments of  $20 \times 20 \mu\text{m}$  in each axis. Each map point was acquired 1 accumulation using 2 s of detector exposure time per accumulation. Spectra were subjected to baseline correction prior to further analysis.

**Attenuated total reflectance – FTIR spectroscopy.** A Nicolet Avatar 360 FTIR spectrometer (Varian Inc., CA) equipped with a DTGS detector and a Harrick MNP-Pro (Pleasantville, NY, USA) attenuated total reflectance (ATR) accessory was used for all the experiments. Each spectrum was collected for 32 scans at a spectral resolution of  $8 \text{ cm}^{-1}$  over the wavenumber range of  $4000\text{--}400 \text{ cm}^{-1}$ . A background spectrum was carried out under the same experimental conditions and was subtracted from each sample spectrum. Spectral data were acquired with EZ-OMNIC software. These conditions are similar to our previous reports.<sup>38,39,46,47</sup>

**In vitro aerosol dispersion performance.** In accordance with USP Chapter <601> specifications on aerosols and using conditions similar to previously reported,<sup>38,39,46,47</sup> the aerosol dispersion performance of SD DMF and co-SD particles was tested using the Next Generation Impactor™ (NGI™) (MSP Corporation, Shoreview, Minnesota, USA) with a stainless steel induction port (USP throat) attachment (NGI Model 170; MSP Corporation) equipped with specialized stainless steel NGI gravimetric insert cups (MSP Corporation) and FDA approved human DPI device HandiHaler® (Boehringer Ingelheim, Ingelheim, Germany). An airflow rate ( $Q$ ) of  $60 \text{ L min}^{-1}$  (adult airflow rate) was adjusted and measured before each experiment using a COPLEY DFM 2000 flow meter (COPLEY Scientific, Nottingham, United Kingdom). The NGI was connected to a COPLEY HCP5 vacuum pump (COPLEY Scientific) through a COPLEY TPK 2000 critical flow controller (COPLEY Scientific). The mass of powder deposited on each stage was quantified by gravimetric method using type A/E glass fiber filters with diameter 55 mm (PALL Corporation, Port Washington, New York) and 75 mm (Advantec, Japan). Quali-V clear HPMC size 3 inhalation grade capsules (Qualicaps, North Carolina) were filled with about 10 mg of powder was used. Three capsules were used in each experiment. *In vitro* aerosolization was done in triplicate ( $n = 3$ ) under ambient conditions.

For the NGI,  $Q = 60 \text{ L min}^{-1}$ , the  $D_{a50}$  aerodynamic cutoff diameter for each NGI stage was calibrated by the



manufacturer and stated as: stage 1 (8.06  $\mu\text{m}$ ); stage 2 (4.46  $\mu\text{m}$ ); stage 3 (2.82  $\mu\text{m}$ ); stage 4 (1.66  $\mu\text{m}$ ); stage 5 (0.94  $\mu\text{m}$ ); stage 6 (0.55  $\mu\text{m}$ ); and stage 7 (0.34  $\mu\text{m}$ ). The emitted dose (ED) was determined as the difference between the initial mass of powder loaded in the capsules and the remaining mass of powder in the capsules following aerosolization. The ED (%) eqn (1) was used to express the percentage of ED based on the total dose (TD) used. The fine particle dose (FPD) was defined as the dose deposited on stages 2 to 7. The fine particle fraction (FPF%) eqn (2) was expressed as the percentage of FPD to ED. The respirable fraction (RF%) eqn (3) was used as the percentage of FPD to total deposited dose (DD) on all impactor stages.

$$\text{Emitted dose (ED\%)} = \frac{\text{ED}}{\text{TD}} \times 100\% \quad (1)$$

$$\text{Fine particle fraction (FPF\%)} = \frac{\text{FPD}}{\text{ED}} \times 100\% \quad (2)$$

$$\text{Respirable fraction (RF\%)} = \frac{\text{FPD}}{\text{DD}} \times 100\% \quad (3)$$

In addition, the mass median aerodynamic diameter (MMAD) of aerosol particles and geometric standard deviation (GSD)

were calculated using a Mathematica (Wolfram Research, Inc., Champaign, IL) program written by Dr. Warren Finlay.

## Statistical analysis

Design of experiments (DoEs) for *in vitro* aerosol performance was conducted using Design Expert® 8.0.7.1 software (Stat-Ease Corporation, Minneapolis, Minnesota). A full factorial design of  $3^1$  for single component spray dried D-Man and a factorial design of  $3^2$  for co-SD systems were designed. Interaction of excipient and process parameter on the performance of the formulation was evaluated using the 3-D surface plot generated from Design Expert®. All experiments were performed in triplicate ( $n = 3$ ). Results are expressed as mean  $\pm$  standard deviation.

## Results

### Scanning electron microscopy (SEM)

Spray dried DMF was successfully produced at 100% pump rate. Co-SD DMF:D-Man powders at various molar compositions with high drug loading were successfully produced at low (25%), medium (50%) and high (100%) pump rates. The particle shape and surface morphology were visualized by SEM for the all raw and spray dried (SD) one-component powders of DMF and D-Man (Fig. 2). All spray dried samples

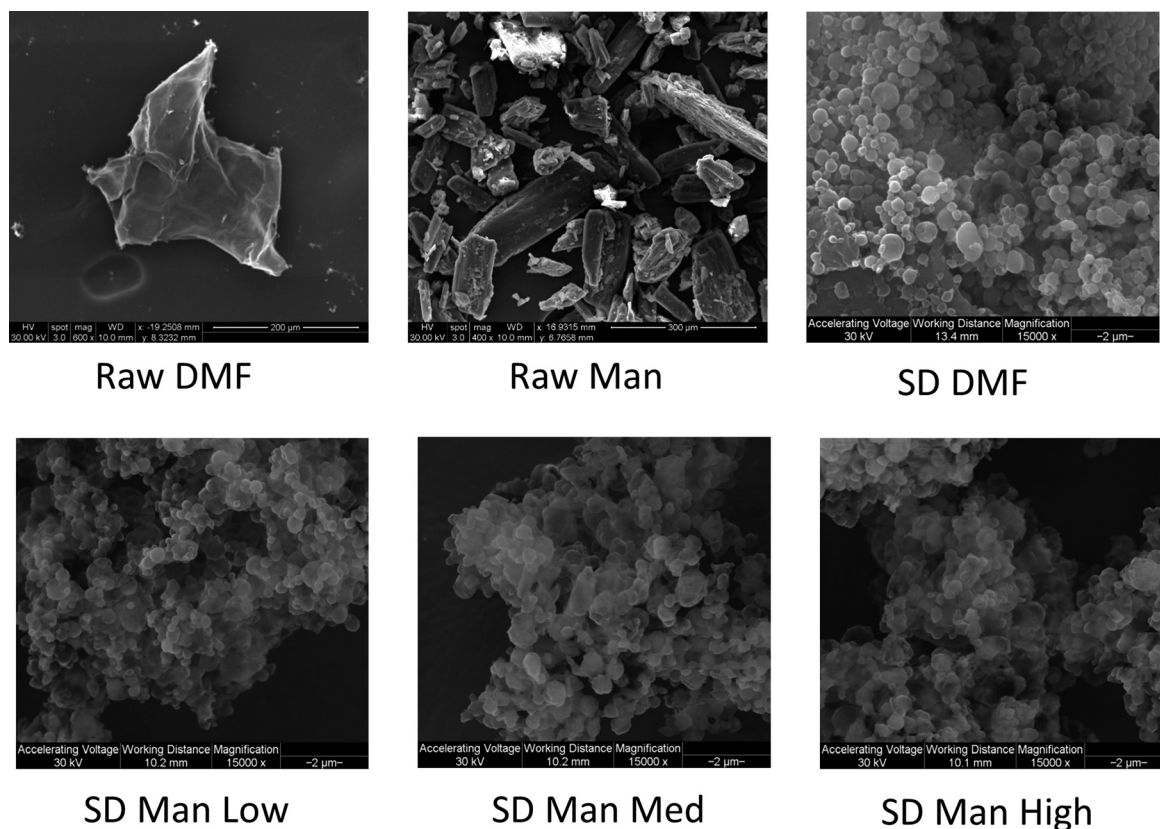


Fig. 2 SEM micrographs of raw DMF, raw D-Man, SD DMF, and SD D-Man.



showed smooth and spherical nanoparticles/nanospheres compared to raw DMF and Man. SD DMF at high pump rate showed smooth and spherical particles and SD D-Man showed spherical particles at low pump rate with slight sintering of particles at medium and high pump rate.

As shown in Fig. 3, co-SD particles at DMF:D-Man 90:10 and 80:20 molar ratios exhibited spherical particles at all pump rates with smooth surface morphology. Co-SD DMF:D-Man 50:50 particles exhibited spherical particles with smooth surface morphology at low pump rates and somewhat crinkled particles at medium & high pump rates.

#### Particle sizing and size distribution by image analysis of SEM micrographs

As shown in Table 2, all co-SD samples had projected mean geometric diameter in the size range of 0.51–1.04  $\mu\text{m}$ , while individually spray dried DMF had 0.76  $\mu\text{m}$  and mannitol had 0.56–1.08  $\mu\text{m}$ . Majority of the particles had a mean geometric

diameter in nanoscale range which is in agreement with the SEM micrographs. All the SD and co-SD particles had particle size range  $\leq 5 \mu\text{m}$ , which is the preferred particle size for inhalation powders.

#### X-Ray powder diffraction (XRPD)

The XRPD pattern of raw DMF showed sharp and intensive peaks characteristic of long-range molecular order (*i.e.* crystallinity) at 2-theta degree values of 10.94, 21.99 and 24.28, as shown in Fig. 4. To the authors knowledge this is the first time powder diffraction pattern of DMF has been reported. The observed peaks are in excellent agreement with predicted powder diffraction pattern obtained using CCDC Cambridge database software. SD DMF had the same pattern as raw DMF suggesting that raw and SD DMF had the same crystal structure. XRPD pattern of D-Man has been previously reported.<sup>46</sup> Comparing with the previous report, the raw D-Man used in this study was found to be beta form with

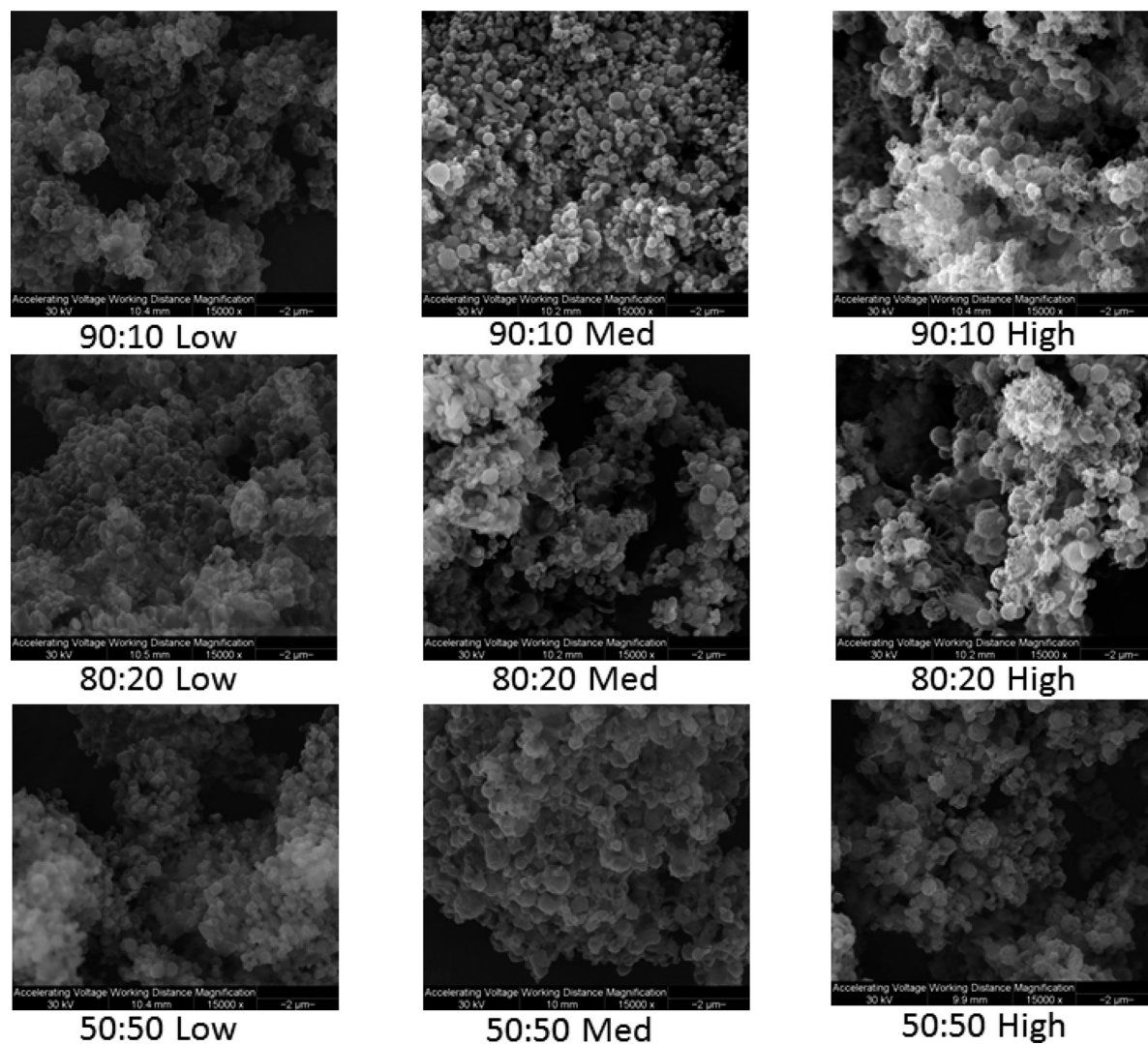


Fig. 3 SEM micrographs of co-SD DMF:D-Man solid-state particles as a function of composition and advanced spray drying pump rate (low, med, and high).





**Table 2** Particle sizing using image analysis on SEM micrographs ( $n \geq 100$  particles)

Powder composition (molar ratio)	Spray drying pump rate (%)	Mean size ( $\mu\text{m}$ )	Size range ( $\mu\text{m}$ )
SD DMF	High (100%)	$0.76 \pm 0.33$	0.18–2.25
Co-SD DMF : D-MAN 90 : 10	Low (25%)	$0.51 \pm 0.16$	0.24–1.00
Co-SD DMF : D-MAN 90 : 10	Med (50%)	$0.56 \pm 0.18$	0.28–1.30
Co-SD DMF : D-MAN 90 : 10	High (100%)	$0.78 \pm 0.29$	0.31–1.74
Co-SD DMF : D-MAN 80 : 20	Low (25%)	$0.58 \pm 0.39$	0.24–3.61
Co-SD DMF : D-MAN 80 : 20	Med (50%)	$0.64 \pm 0.32$	0.22–2.09
Co-SD DMF : D-MAN 80 : 20	High (100%)	$0.84 \pm 0.37$	0.27–2.29
Co-SD DMF : D-MAN 50 : 50	Low (25%)	$0.54 \pm 0.18$	0.23–0.98
Co-SD DMF : D-MAN 50 : 50	Med (50%)	$1.04 \pm 0.47$	0.34–2.93
Co-SD DMF : D-MAN 50 : 50	High (100%)	$1.01 \pm 0.45$	0.31–2.66
SD D-MAN	Low (25%)	$0.56 \pm 0.25$	0.21–1.33
SD D-MAN	Med (50%)	$1.08 \pm 0.62$	0.39–3.12
SD D-MAN	High (100%)	$0.80 \pm 0.45$	0.27–2.71

prominent peaks at 18.77, 23.39, 14.65 and 20.47 2-theta degree values. However, SD D-Man exhibited peaks at different 2-theta degree values. The diffraction pattern of SD D-Man closely resembles that of alpha and delta polymorphic forms

at all three pump rates. Li *et al.* observed alpha (medium pump rate) and alpha and delta (high pump rate) polymorphic forms at the same pump rate.<sup>46</sup> However, it is worth mentioning that the inlet and outlet temperatures were

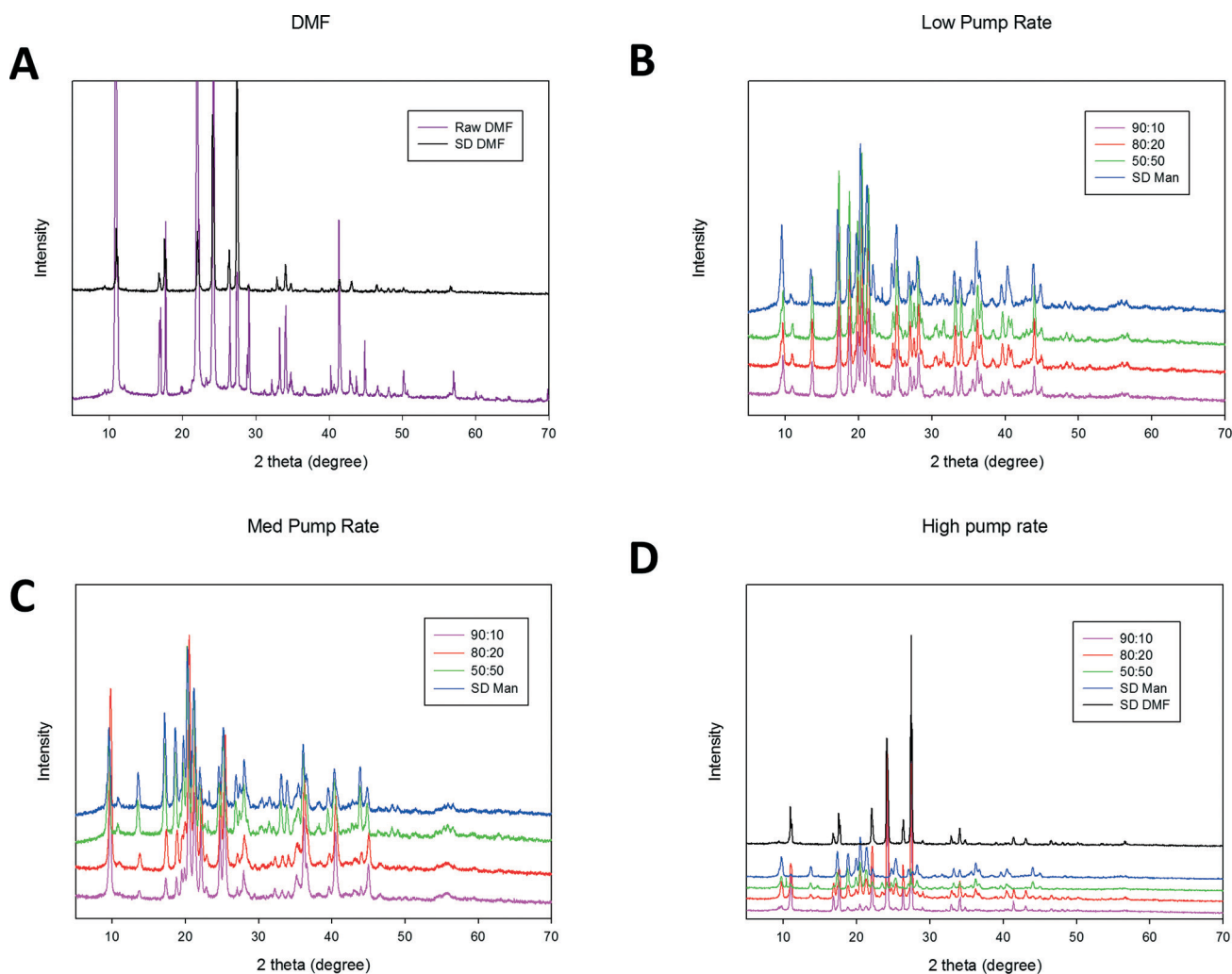


**Fig. 4** XRPD diffraction patterns for: (A). raw and SD DMF powders; (B). Co-SD DMF : D-Man and SD D-Man powders designed at low spray drying pump rate; (C). Co-SD DMF : D-Man and SD D-Man powders designed at medium spray drying pump rate; and (D). Co-SD DMF : D-Man and SD D-Man designed at high spray drying pump rate.



different in both the studies. The rich diffraction pattern seen in both the samples (DMF and D-Man) suggest that the single components possessed long range molecular order and this was retained after spray drying.

For the co-SD DMF:D-Man powders, all XRPD diffractograms exhibited sharp peaks which are characteristic of long-range molecular order *i.e.* crystallinity, as shown in Fig. 4. The diffraction pattern of co-SD samples (all three molar ratios) were similar to SD D-Man at low and medium pump rates. At high pump rate, 90:10 had diffraction pattern similar to SD DMF while other two molar ratios had mixed pattern resembling both DMF and D-Man.

All spray dried and co-spray dried samples exhibited several sharp peaks characteristic of long range molecular order, which is consistent with highly crystalline powders. Unlike majority of spray dried systems which forms amorphous dispersion, the presence of sharp peaks in spray dried and co-SD samples is indicative of retention of crystallinity following organic solution closed mode spray drying. Retention of crystallinity by mannitol following spray drying was recently reported by Li *et al.*<sup>46</sup>

### Differential scanning calorimetry (DSC)

Representative DSC thermograms of raw components, SD single component and co-spray dried particles are shown in Fig. 5. Raw and SD DMF exhibit single endothermic transition at about 102 °C suggesting transition from ordered to

disordered phase. The presence of ordered phase at room temperature is in good agreement with XRPD data. Raw and SD D-Man exhibited single transition similar to previously reported results.<sup>46</sup> As can be seen from Table 3, an increase in enthalpy was observed for SD D-Man samples with an increase in pump rate. There was a spray drying pump rate effect observed on the DSC thermograms of co-SD particles. At low and medium pump rates, there was only one endothermic transition at about 164 °C, while at high pump rate two endothermic transitions were observed at 102 °C and 164 °C. At room temperature, all co-SD particles exhibited no transition suggesting existence of ordered phase that is consistent with XRPD observation. At higher heating scan rates of 20 °C min<sup>-1</sup> and 40 °C min<sup>-1</sup>, there was no reproducible transition (glass) or no transition observed for all the samples (data not shown). The two endothermic peaks observed at high pump rate suggest decreased molecular miscibility between the two components at that pump rate (100%) while single peak at lower pump rates suggest molecular encapsulation of the drug in the excipient (D-Man). In any case, from all DSC data it is clear that the components exist in crystalline ordered phase before and after spray drying suggesting absence of polymorphic interconversion.

### HSM under cross-polarizer lens

Fig. 6 shows representative images from HSM experiment. All raw samples exhibited birefringence suggestive of crystallinity

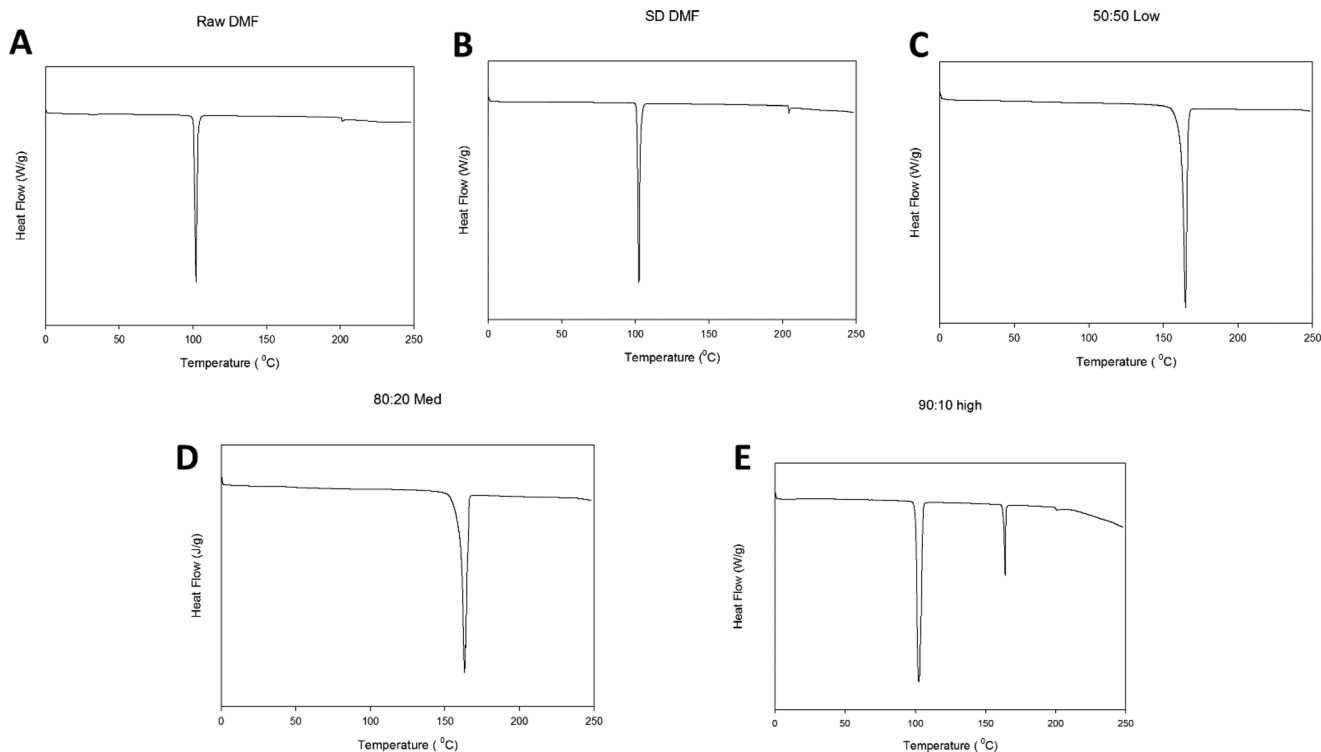


**Fig. 5** Representative DSC thermograms for: (A). raw DMF; (B). SD DMF; (C). Co-SD DMF:D-Man 50:50 designed at low spray drying pump rate; (D). Co-SD DMF:D-Man 80:20 designed at medium spray drying pump rate; and (E). Co-SD DMF:D-Man 90:10 designed at high spray drying pump rate.



**Table 3** DSC thermal analysis ( $n = 3$ , mean  $\pm$  standard deviation)

Powder composition (molar ratio)	Spray drying pump rate (%)	$T_{\text{peak}}$ ( $^{\circ}\text{C}$ )	$\Delta H$ ( $\text{J g}^{-1}$ )
Raw DMF	N/A	$102.19 \pm 0.02$	$245.3 \pm 37.26$
Raw D-MAN	N/A	$166.39 \pm 0.06$	$316.97 \pm 3.02$
SD DMF	High (100%)	$102.12 \pm 0.21$	$242.133 \pm 7.73$
Co-SD DMF : D-MAN 90 : 10	Low (25%)	$164.08 \pm 0.10$	$308.67 \pm 124.91$
Co-SD DMF : D-MAN 90 : 10	Med (50%)	$163.78 \pm 0.03$	$303.57 \pm 19.49$
Co-SD DMF : D-MAN 90 : 10	High (100%)	$102.90 \pm 0.26$	$231.57 \pm 11.48$
		$164.34 \pm 0.19$	$33.88 \pm 1.79$
Co-SD DMF : D-MAN 80 : 20	Low (25%)	$163.87 \pm 0.04$	$290.03 \pm 2.67$
Co-SD DMF : D-MAN 80 : 20	Med (50%)	$163.36 \pm 0.22$	$286.00 \pm 3.01$
Co-SD DMF : D-MAN 80 : 20	High (100%)	$102.08 \pm 0.19$	$154.93 \pm 0.27$
		$164.08 \pm 0.04$	$96.09 \pm 17.35$
Co-SD DMF : D-MAN 50 : 50	Low (25%)	$164.69 \pm 0.19$	$233.83 \pm 18.14$
Co-SD DMF : D-MAN 50 : 50	Med (50%)	$164.99 \pm 0.19$	$267.37 \pm 20.46$
Co-SD DMF : D-MAN 50 : 50	High (100%)	$100.26 \pm 0.44$	$11.22 \pm 1.22$
		$164.61 \pm 0.51$	$286.50 \pm 35.27$
SD D-MAN	Low (25%)	$164.92 \pm 0.12$	$251.33 \pm 6.98$
SD D-MAN	Med (50%)	$163.32 \pm 0.17$	$285.17 \pm 27.24$
SD D-MAN	High (100%)	$164.06 \pm 0.10$	$366.13 \pm 57.10$

of the particles. Raw DMF at increasing temperature started melting at about  $80^{\circ}\text{C}$  and completely melted at  $100^{\circ}\text{C}$ . However, there was particle growth observed for SD DMF sample from  $70$ – $102^{\circ}\text{C}$  followed by melting starting at  $103.7^{\circ}\text{C}$  and completely melted at  $104.5^{\circ}\text{C}$ . This is an unusual phenomenon observed on heating SD DMF particles, which can be attributed to transition to a different phase. However, this needs further investigation. Raw D-Man and SD D-Man (all pump rates) exhibited one observable transition from solid state to liquid state at temperatures higher than  $160^{\circ}\text{C}$ . However, different co-SD particles showed thermal events on heating. All low and medium pump rate particles showed one transition from solid state to liquid state at higher temperatures of  $160$ – $166^{\circ}\text{C}$ . At high pump rate all co-SD samples had two observable thermal events upon heating. One was loss of birefringence which can be described as melting of one component at about  $60$ – $70^{\circ}\text{C}$  and other melting at  $160$ – $164^{\circ}\text{C}$ . Additionally,  $80:20$  molar ratio particles at  $100\%$  pump rate showed a particle growth similar to SD DMF starting at  $70^{\circ}\text{C}$ . The thermal activity observed with HSM is comparable with the DSC data, where two peaks were seen at high pump rate and one peak seen at low and medium pump rates.

#### Karl Fisher titration (KFT)

Table 4, shows the residual water content in the raw and spray dried powders. The SD D-Man samples had low water content but higher than raw D-Man. This is similar to previously reported residual water content results of D-mannitol before and after spray drying. It can be noted from the Table 4 that all SD powder samples had residual water content  $\leq 1.50\%$  w/w. These values of residual water content are considered acceptable for inhalation dry powder formulation.

#### ATR-FTIR spectroscopy

ATR-FTIR spectra in Fig. 7, confirms the presence of the components in the co-SD particles. The spectra of DMF obtained

is similar to the spectra reported in Scifinder® and by Lopes *et al.*<sup>49</sup> Co-SD samples at the low and medium spray drying pump rates showed O–H stretching at  $3260$ – $3280\text{ cm}^{-1}$  suggesting H-bonding with D-mannitol. At high pump rate, the spectra are similar to SD DMF. Additionally,  $80:20$  at low and medium samples shows C–H stretch at  $2940\text{ cm}^{-1}$ .

#### Confocal Raman microspectroscopy (CRM), chemical imaging, & mapping

Confocal Raman microscopy analysis was performed to further investigate the physical form and homogeneity of DMF and Man in co-SD particles. A spectral scan from  $100$ – $4000\text{ cm}^{-1}$  was performed on all samples. All the samples exhibited high crystallinity before and after spray drying with or without D-Man. Based on the spectral scan of both the components, Raman shift in the range of  $2826$ – $3289\text{ cm}^{-1}$  was observed during confocal Raman mapping (CRM). In general, the spectral scan and CRM of all samples were in good agreement. As seen in Fig. 8 and 9, the spectral scan of all co-SD samples at low pump rate exhibited Raman shift that was consistent with D-Man. At medium pump rate,  $90:10$  molar ratio sample showed Raman shift of both DMF and D-Man while other samples exhibited only that of D-Man. At high pump rate, co-SD DMF : D-Man  $90:10$  and  $80:20$  powders had Raman shift consistent with that of DMF while  $50:50$  exhibited that of Man. Interestingly, co-SD DMF : D-Man  $50:50$  powder exhibited Raman spectra similar to that of D-Man. By CRM, all co-spray dried samples (all molar ratios and all pump rates) exhibited homogeneity in their distribution. Fig. 10 shows representative brightfield micrographs obtained at  $20\times$  magnification of co-SD samples and the corresponding Raman signal obtained from different regions of the imaged sample. The image represents an area of the powder sample to assess the chemical composition (*i.e.* molecular fingerprint) and distribution of the components. As can be seen from





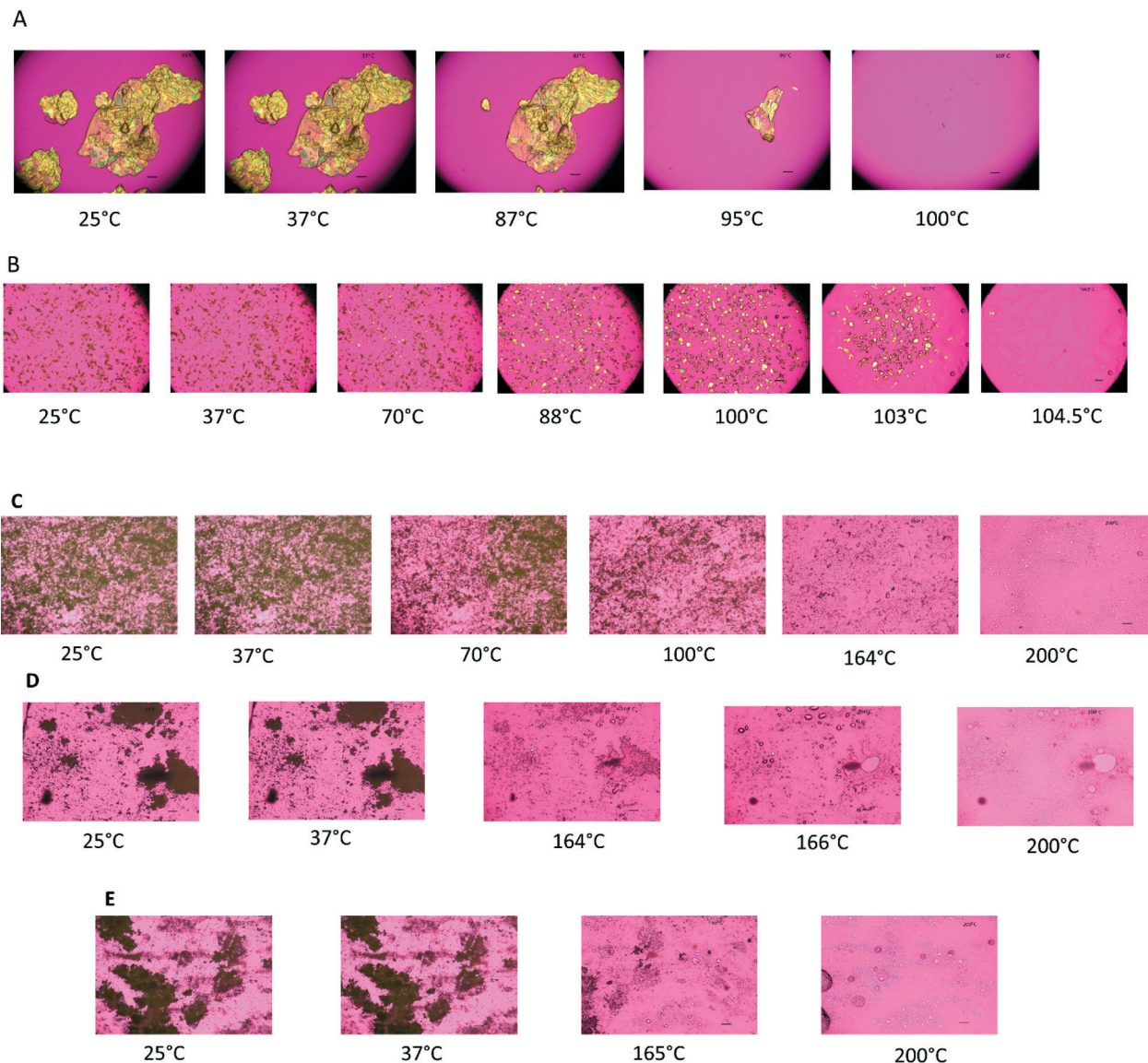


**Fig. 6** Representative HSM images for: (A). Raw DMF; (B). SD DMF; (C). Co-SD DMF:D-Man 90:10 designed at high spray drying pump rate; (D). Co-SD DMF:D-Man 80:20 designed at medium spray drying pump rate; and (E). Co-SD DMF:D-Man 50:50 designed at low spray drying pump rate.

Fig. 10A and B, the peaks are consistently seen in a given sample suggesting uniform distribution of the components. Fig. 10A exhibits the characteristic peaks corresponding to DMF, while Fig. 10B exhibits the characteristic peaks of D-Man. Raman spectra of co-SD samples at some pump rates showed peaks corresponding to mannitol at different molar ratios suggesting encapsulation of the drug by mannitol.

### *In vitro* aerosol dispersion performance

*In vitro* aerosol dispersion performance using NGI® revealed that all SD and co-SD systems had high ED values. For most of the co-SD DMF:D-Man systems, the FPF was improved with the addition of the aerosol performance enhancer,

D-Man, compared to the one-component SD DMF powders. Aerosol dispersion of SD DMF alone exhibited higher fraction of particle deposition at the earlier stages (1–3), but inclusion of D-Man had profound effect on the stage deposition. As can be seen from the Fig. 11, co-spray drying DMF with D-Man decreased the deposition on stage 2, but increased the aerosol deposition on stages 1 and 3–6, which include nanoparticles in the solid state. There was no measurable deposition seen on stage 7 for all aerosolized powders.

## Discussion

To the authors' knowledge, this is the first reported study to successfully design and optimize DPIs of DMF and DMF:D-Man molecular mixtures by organic solution advanced



**Table 4** Residual water content quantified by KFT ( $n = 3$ , mean  $\pm$  standard deviation)

Powder composition (molar ratio)	Spray drying pump rate (%)	Residual water content (% w/w)
Raw DMF	N/A	$0.26 \pm 0.05$
Raw D-MAN	N/A	$0.21 \pm 0.01$
SD DMF	High (100%)	$0.16 \pm 0.01$
Co-SD DMF : D-MAN 90 : 10	Low (25%)	$1.36 \pm 0.04$
Co-SD DMF : D-MAN 90 : 10	Med (50%)	$1.05 \pm 0.05$
Co-SD DMF : D-MAN 90 : 10	High (100%)	$0.37 \pm 0.04$
Co-SD DMF : D-MAN 80 : 20	Low (25%)	$1.26 \pm 0.07$
Co-SD DMF : D-MAN 80 : 20	Med (50%)	$0.82 \pm 0.09$
Co-SD DMF : D-MAN 80 : 20	High (100%)	$0.48 \pm 0.08$
Co-SD DMF : D-MAN 50 : 50	Low (25%)	$1.20 \pm 0.06$
Co-SD DMF : D-MAN 50 : 50	Med (50%)	$1.49 \pm 0.16$
Co-SD DMF : D-MAN 50 : 50	High (100%)	$1.61 \pm 0.08$
SD D-MAN	Low (25%)	$1.46 \pm 0.06$
SD D-MAN	Med (50%)	$0.79 \pm 0.21$
SD D-MAN	High (100%)	$0.98 \pm 0.01$

closed mode spray drying. This study is also the first to have comprehensively characterized DMF for its physicochemical properties in the solid state. The systematic approach in this study included single component SD drug, single component SD excipient (D-Man) and co-SD rationally chosen molar ratios of drug:excipient. Particle engineering techniques are often used in inhalation formulation to achieve narrow particle

size distribution, small, smooth particles, hollow or encapsulated particles which can be aerosolized without a carrier. Spray drying is the most versatile particle engineering design technology particularly when using dilute organic solutions in closed mode advanced spray drying<sup>50</sup> leading to small, spherical and dry particles that can successfully target the lower airways, as reported by us.<sup>37,46,47,51–55</sup>

This study shows that the presence of D-Man in the solution has enabled DMF molecules to be encapsulated into small, spherical particles at lower pump rates while DMF didn't form particles at these pump rates individually. This is likely due to the hydrogen bonding between DMF and D-Man, since D-Man is an H-bond donor and DMF is an H-bond acceptor. In solution polar organic molecules tends to form hydrogen bonded aggregates, these aggregates serve to be the precursor for the crystal of the molecules. SEM micrographs of SD particles has shown diameter  $<2 \mu\text{m}$  which is the preferred particle size for targeted delivery to deeper regions of lung. The size and shape of particles determines the forces that the particle will experience during its fluid motion (*i.e.* aerosolization).<sup>56</sup> By targeting in this manner, the dose of the drug that needs to be inhaled can be reduced. This is also the rationale in choosing the DMF:D-Man molar ratios in this study, where the ratio of Man was not to exceed that of the drug, as high drug loading is desired for DPI delivery. But, in this study the DMF

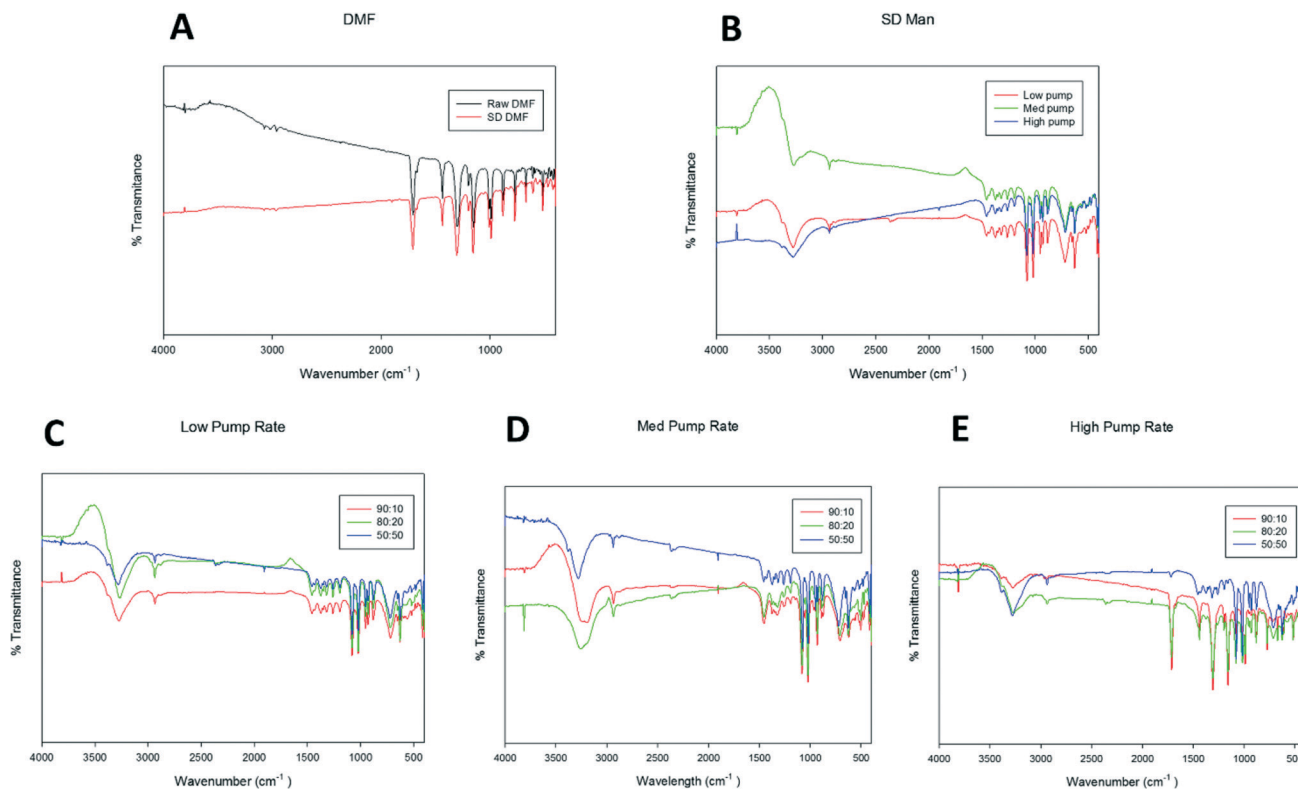


**Fig. 7** ATR-FTIR spectra for: (A). raw and SD DMF; (B). SD D-Man designed at three spray drying pump rates of low, medium, and high; (C) co-SD DMF : D-Man powders designed at low spray drying pump rate; (D) co-SD DMF : D-Man powders designed at medium spray drying pump rate; and (E). co-SD DMF : D-Man powders designed at high spray drying pump rate.



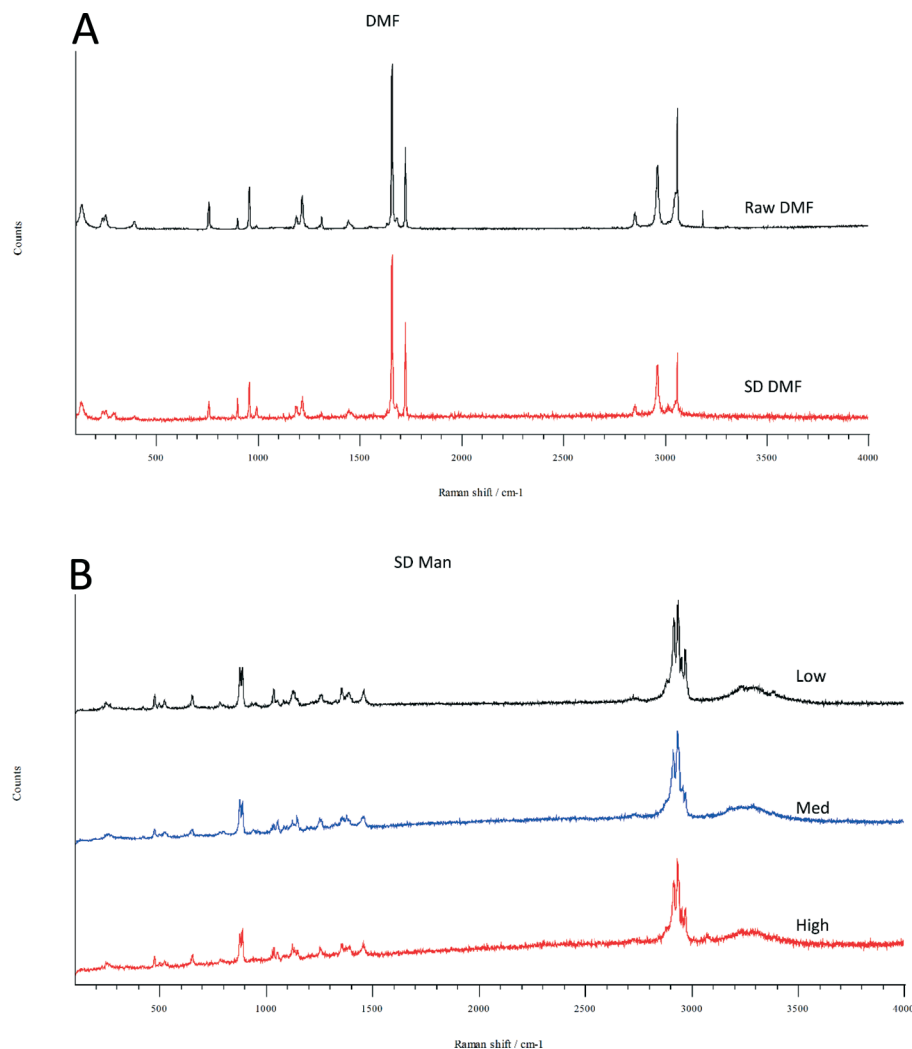


**Fig. 8** Raman spectra for one-component powders for: (A). raw DMF and SD DMF; and (B). SD D-Man designed at three spray drying pump rates (low, medium, and high).

individually and co-SD with D-Man retained its crystallinity and this is evident from DSC, XRPD and Raman analysis. However, the DSC thermograms of co-SD particles showed different miscibility among the components at different pump rates. The single transition observed at low and medium pump rates suggest that the components were homogenous and completely miscible on a molecular level, while two transitions seen at high pump rate suggest molecular heterogeneity such as nanodomains. At low and medium pump rates, the drying process is slower, while at a higher pump rate the drying process is faster. Hence, longer spray drying time during low and medium pump rates can promote miscibility of the components in the solid state. This is verified by the HSM images where melting of two components sequentially was noticed at only high pump rate.

This can be due to the favorable H-bonding of the two components at lower pump rates as seen from ATR-FTIR analysis. DMF is a symmetrical molecule that can exist in

several different isomeric forms. The most stable conformer is reported to have both ester groups in *cis* orientation with respect to the C=C bond.<sup>49</sup> The energy difference seen in DSC can be due to the conformational changes of the molecule at that pump rate. All thermal analysis confirmed the stability of the particles at room temperature and biological temperature. However, the particle growth observed in HSM of SD DMF at higher temperature needs further investigation. Dry powder aerosol particles are not expected to be exposed to higher temperatures (70 °C or higher), hence the investigation is reserved for future study. The crystalline nature of the SD particles was further verified by the low residual water content of all the particles. The crystallinity of the particle with low water content can lead to increased physical and chemical stability of the powder for a prolonged period of time. Crystalline compounds possess less molecular mobility which leads to decreased reactivity, hence increased physical and chemical stability. Additionally, decreased residual water can lead to better aerosol dispersion performance.





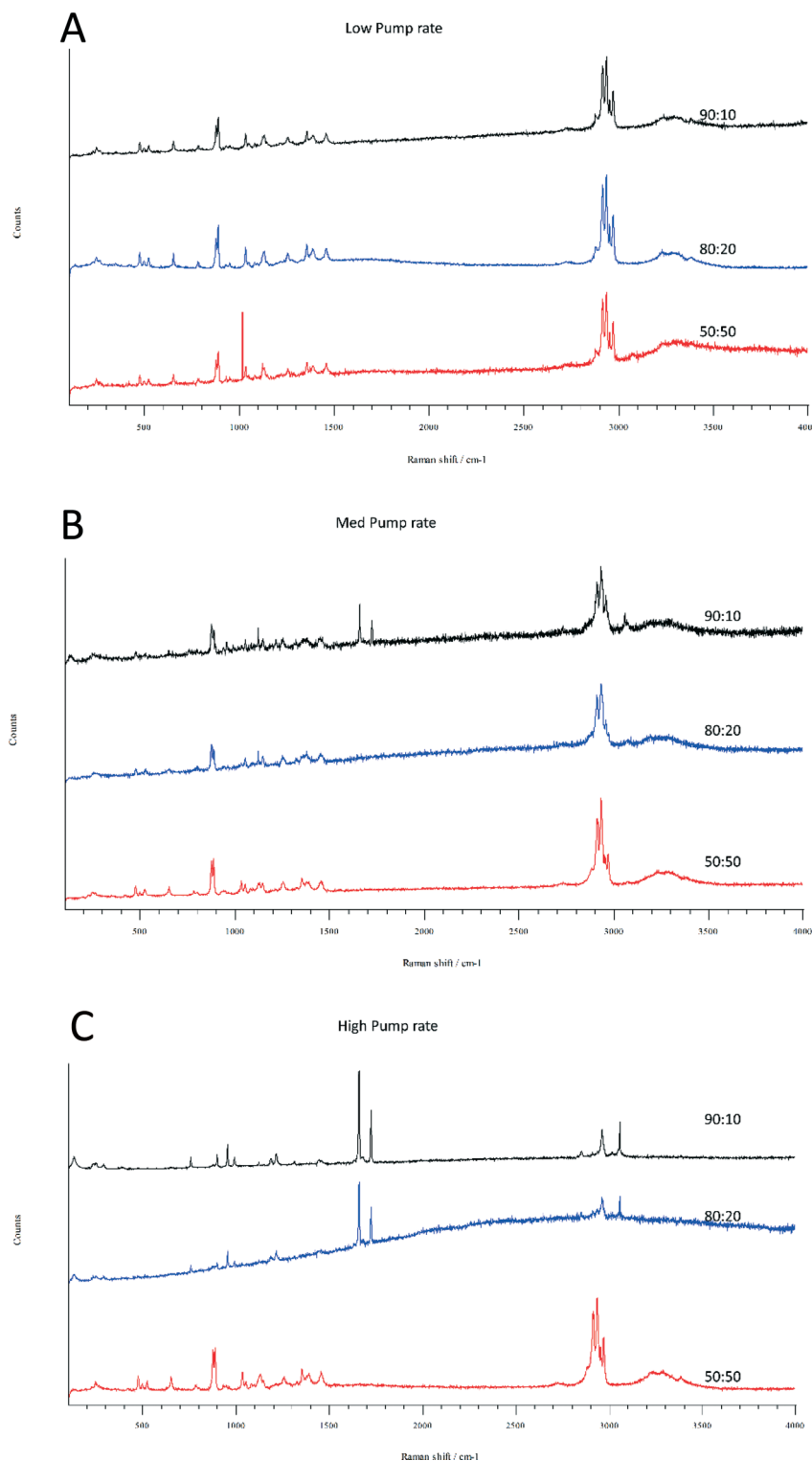
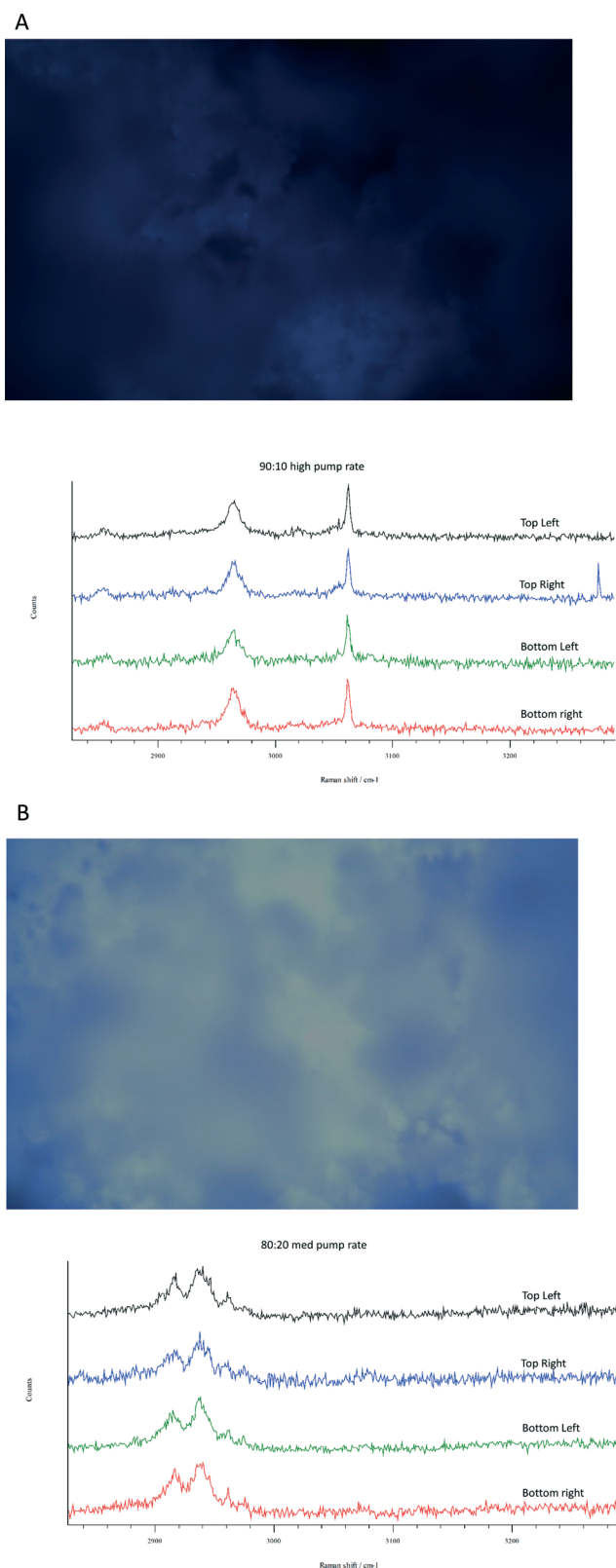


Fig. 9 Raman spectra of co-SD DMF:D-Man powders designed at three spray drying pump rates as: (A). low spray drying pump rate; (B). medium spray drying pump rate; and (C). high spray drying pump rate.

The *in vitro* aerosol performance of the spray dried and co-SD systems are tabulated in Table 5 and the influence of pump rate and D-Man concentration is presented in 3-D surface response plots (DesignExpert®) in Fig. 12. Co-SD 50:50 system, high pump rate had the highest EDF, FPF and RF

and minimum MMAD, followed by low pump rate and medium pump. Co-SD 80:20 system, exhibited a trend as can be seen in Fig. 12, where EDF, FPF and RF increased as the pump rate increased and MMAD decreased as the pump rate decreased. Co-SD 90:10, low pump rate showed lower EDF,





**Fig. 10** Representative confocal Raman microspectroscopy for chemical imaging and mapping for co-SD DMF:D-MAN inhalable powders for: (A). DMF:D-MAN 90:10 designed at high spray drying pump rate showing peaks of DMF and D-D-MAN; and (B). DMF:D-MAN 80:20 designed at medium spray drying pump rate showing peaks of D-MAN.

FPF, and RF and higher MMAD compared to other two pump rates. However, the performance values of medium and high pump rates are comparable. Similar to 50:50 co-SD system, SD D-Man high pump rate had the highest EDF, FPF and RF and minimum MMAD, followed by low pump rate and medium pump.

Compared to single component SD DMF, the emitted dose fraction was increased only in some of the systems with increased DMF concentration and higher pump rate (80:20 50%, 80:20 100% and all pump rates of 90:10 ratio). Except, 50:50 ratio at 50% pump rate all other co-SD systems had increased FPF. However, RF of particles wasn't increased in systems other than 50:50 100% and 80:20 100%. Some co-SD systems decreased the MMAD while others had increased value. All ratios at 100% pump rate had lower or comparable MMAD to single component SD-DMF. At 25% pump rate only 50:50 molar ratio co-SD system had MMAD less than SD-DMF. At 50% molar ratios with lower mannitol (80:20 and 90:10) had MMAD less than or comparable to SD-DMF. The effect of pump rate and different concentration of mannitol was studied using the 3-D surface response graphs (Fig. 12) generated from Design Expert® software. Overall, 50:50 molar ratio at 100% pump rate had the highest FPF, RF and lowest MMAD which may be due to the presence of D-Man, because at 100% pump rate SD D-Man at 100% pump rate had similar characteristics. However, ED was highest at 80:20 high pump rate and GSD lowest of single component SD DMF.

The aerosol stage deposition in Fig. 11, demonstrated using NGI and Handihaler device indicate that the formulation possess the capability to reach lower airways of the lung. The deposition of the aerosol particles at this region is characterized by sedimentation and Brownian diffusion in addition to the low air velocity.<sup>57</sup> Inflammatory diseases such as asthma and COPD are characterized by airway remodeling and the pathological process involves both larger and smaller airways. However the difference between these two diseases lie in the cells that are involved in the process. In COPD, CD8+, T-lymphocytes and macrophages are the predominant cells involved.<sup>58</sup> Hence, targeted delivery of DMF to this respiratory region will be advantageous in targeting the underlying mechanisms giving rise to pulmonary inflammation because it possesses both anti-inflammatory and anti-oxidant properties. Additionally, the hydrophobicity of DMF would be expected to increase drug residence time in the lungs due to favorable hydrophobic interactions with lung cellular membranes. This, in turn, would be expected to decrease dosing frequency administration of the drug. DMF hydrophobicity would also be expected to minimize drug translocation out of the lung, thereby decreasing systemic side effects.

## Conclusions

This systematic and comprehensive study reports for the first time on the successful design of advanced inhalable dry powders containing DMF, a first-in-class Nrf2 activator



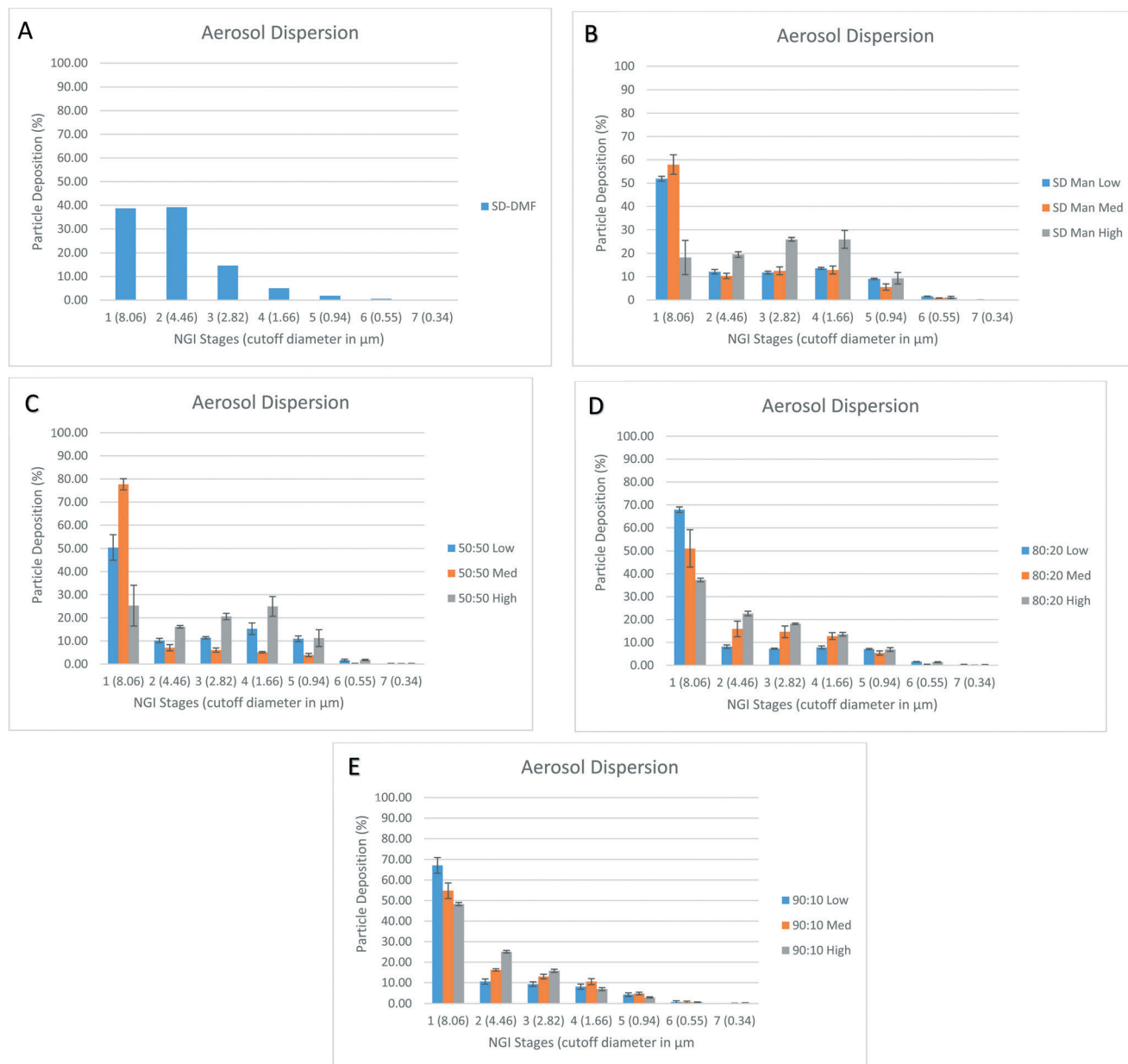


**Fig. 11** *In vitro* aerosol dispersion performance as DPIs using the NGI and the FDA-approved human DPI device, the Handihaler® for: (A). SD DMF; (B). SD D-Man; (C). Co-SD DMF : D-Man 50 : 50; (D). Co-SD DMF : D-Man 80 : 20; and (E). Co-SD DMF : D-Man 90 : 10.

**Table 5** *In vitro* aerosol dispersion performance as DPIs ( $n = 3$ , mean  $\pm$  standard deviation)

Powder formulation composition (molar ratio)	Spray drying pump rate (%)	Emitted dose (%)	Fine particle fraction (%)	Respirable fraction (%)	MMAD ( $\mu\text{m}$ )	GSD
SD DMF	High (100%)	85.18 $\pm$ 5.51	17.07 $\pm$ 4.72	61.28 $\pm$ 21.61	7.59 $\pm$ 1.55	1.89 $\pm$ 0.16
SD D-MAN	Low (25%)	89.57 $\pm$ 4.05	29.56 $\pm$ 3.83	43.26 $\pm$ 6.02	7.24 $\pm$ 1.68	2.81 $\pm$ 0.20
SD D-MAN	Med (50%)	81.55 $\pm$ 8.59	26.34 $\pm$ 3.46	37.60 $\pm$ 4.28	8.56 $\pm$ 1.34	2.84 $\pm$ 0.18
SD D-MAN	High (100%)	85.89 $\pm$ 10.38	49.46 $\pm$ 6.93	76.15 $\pm$ 6.01	3.89 $\pm$ 0.34	1.98 $\pm$ 0.32
DMF : D-MAN 50 : 50	Low (25%)	69.60 $\pm$ 10.52	33.63 $\pm$ 2.06	49.59 $\pm$ 5.47	5.32 $\pm$ 0.81	2.59 $\pm$ 0.15
DMF : D-MAN 50 : 50	Med (50%)	64.59 $\pm$ 7.35	13.64 $\pm$ 1.94	22.33 $\pm$ 2.41	18.36 $\pm$ 1.87	3.73 $\pm$ 0.18
DMF : D-MAN 50 : 50	High (100%)	71.64 $\pm$ 15.20	42.56 $\pm$ 1.32	74.73 $\pm$ 8.82	3.67 $\pm$ 0.59	2.01 $\pm$ 0.13
DMF : D-MAN 80 : 20	Low (25%)	84.08 $\pm$ 10.30	22.63 $\pm$ 0.82	32.10 $\pm$ 1.19	10.92 $\pm$ 0.74	3.69 $\pm$ 0.18
DMF : D-MAN 80 : 20	Med (50%)	88.70 $\pm$ 3.10	29.82 $\pm$ 4.53	48.96 $\pm$ 8.11	6.86 $\pm$ 1.25	2.46 $\pm$ 0.17
DMF : D-MAN 80 : 20	High (100%)	95.66 $\pm$ 4.69	34.48 $\pm$ 1.42	62.70 $\pm$ 0.81	5.56 $\pm$ 0.26	2.38 $\pm$ 0.05
DMF : D-MAN 90 : 10	Low (25%)	85.17 $\pm$ 5.61	23.15 $\pm$ 1.76	32.89 $\pm$ 3.83	11.15 $\pm$ 1.84	3.09 $\pm$ 0.15
DMF : D-MAN 90 : 10	Med (50%)	87.74 $\pm$ 6.30	24.12 $\pm$ 2.43	45.23 $\pm$ 3.79	7.85 $\pm$ 0.92	2.65 $\pm$ 0.14
DMF : D-MAN 90 : 10	High (100%)	87.01 $\pm$ 7.58	24.15 $\pm$ 0.83	51.70 $\pm$ 0.77	7.86 $\pm$ 0.33	2.34 $\pm$ 0.07





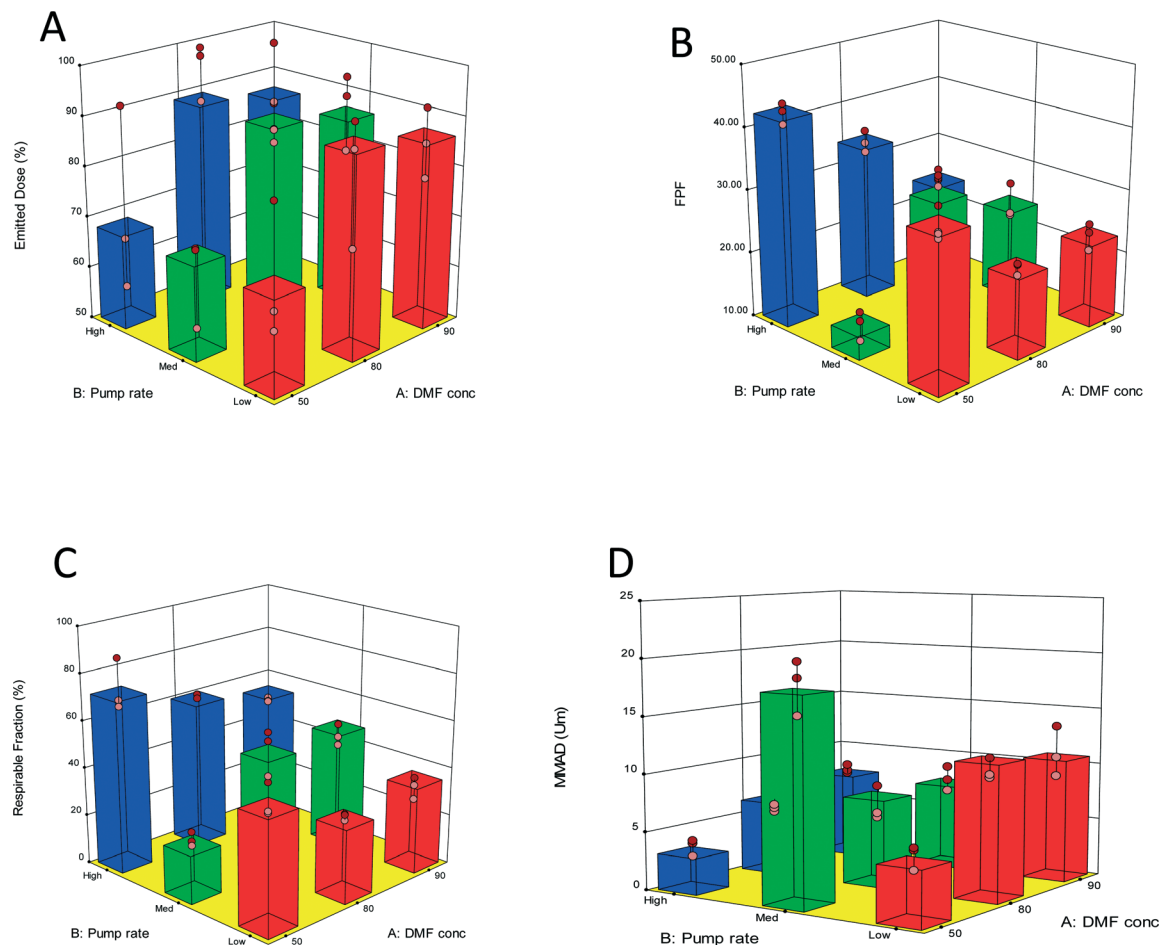


Fig. 12 3-D surface response plots showing the influence of spray drying pump rate (a pharmaceutical processing property) and chemical composition (a molecular property) on *in vitro* aerosol dispersion performance (a macroscopic performance property) as DPIs for: (A). ED; (B). FPF; (C). RF; and (D). MMAD.

drug to treat pulmonary inflammation, using advanced particle engineering design technology for targeted delivery to the lungs as advanced spray dried one-component DPIs. In addition, two-component co-spray dried (co-SD) DMF : D-Man DPIs with high drug loading were successfully designed for targeted lung delivery as advanced DPIs using organic solution advanced spray drying in closed mode. Regional targeted deposition using *in vitro* predictive lung modeling based on aerodynamic properties was tailored based on composition and spray drying parameters. These findings indicate the significant potential of using D-Man in spray drying to improve particle formation and aerosol performance of small molecule with a relatively low melting point. These respirable microparticles/nanoparticles in the solid-state exhibited excellent aerosol dispersion performance with a human DPI device. Using *in vitro* predictive lung deposition modeling, the aerosol deposition patterns of these particles show the capability to reach lower airways to treat inflammation in this region in pulmonary diseases such as ALI/ARDS, COPD, PH, and pulmonary endothelial disease.

## Acknowledgements

The authors sincerely thank Professor Shyam Biswal at The Johns Hopkins University Bloomberg School of Public Health for very helpful discussions and insights into DMF and Nrf2 mechanisms in the lungs. The authors gratefully acknowledge financial support from the College of Pharmacy graduate student fellowship awarded to PM. This work was partially supported by the NIH NIAID (subaward to HMM, PI at The UA). The authors thank Dr. Brooke Beam Masani (SEM), Dr. Sue Roberts (XRPD) at the KECK imaging facility, Dr. Paul Wallace (Raman) at USIF and Dr. Chad Park (ATR-FTIR) at The University of Arizona for access to core facilities. PM thanks Mr. Sriram Srinivasan for his assistance.

## References

- 1 P. Muralidharan, D. Hayes, Jr. and H. M. Mansour, *Expert Opin. Drug Delivery*, 2015, 12, 947–962.
- 2 N. Angelis, K. Porpodis, P. Zarogoulidis, D. Spyrtatos, I. Kioumis, A. Papaiwannou, G. Pitsiou, K. Tsakiridis, A.



- Mpakas, S. Arikas, T. Tsiouda, N. Katsikogiannis, I. Kougioumtzi, N. Machairiotis, M. Argyriou, G. Kessisis and K. Zarogoulidis, *J. Thorac. Dis.*, 2014, 6(Suppl 1), S167–172.
- 3 M. Anna, *Asthma in Focus*, Pharmaceutical Press/ RPS publishing, London, UK, 2007.
  - 4 A. S. Buist, *Eur. Respir. J.*, 2003(Supplement 39), 30s–35s.
  - 5 R. M. Pascual and S. P. Peters, in *Asthma and COPD: basic mechanisms and clinical management*, ed. P. J. Barnes, J. M. Drazen, S. I. Rennard and N. C. Thomson, Academic Press/ Elsevier, San Diego, CA, USA, 2009, pp. 763–774.
  - 6 P. Seidel, I. Merfort, J. M. Hughes, B. G. Oliver, M. Tamm and M. Roth, *Am. J. Physiol.*, 2009, 297, L326–339.
  - 7 V. M. Reddy, B. Meyrick, J. Wong, A. Koor, J. R. Liddicoat, F. L. Hanley and J. R. Fineman, *Circulation*, 1995, 92, 606–613.
  - 8 S. Fratz, J. R. Fineman, A. Gorlach, S. Sharma, P. Oishi, C. Schreiber, T. Kietzmann, I. Adatia, J. Hess and S. M. Black, *Circulation*, 2011, 123, 916–923.
  - 9 R. M. Tuder, B. Groves, D. B. Badesch and N. F. Voelkel, *Am. J. Pathol.*, 1994, 144, 275–285.
  - 10 S. Hall, P. Brogan, S. G. Haworth and N. Klein, *Thorax*, 2009, 64, 778–783.
  - 11 L. A. Shimoda and S. S. Laurie, *J. Appl. Physiol.*, 2014, 116, 867–874.
  - 12 S. Sharma, S. Kumar, N. Sud, D. A. Wiseman, J. Tian, I. Rehmani, S. Datar, P. Oishi, S. Fratz, R. C. Venema, J. R. Fineman and S. M. Black, *Vasc. Pharmacol.*, 2009, 51, 359–364.
  - 13 L. A. Gabrielli, P. F. Castro, I. Godoy, R. Mellado, R. C. Bourge, H. Alcaino, M. Chiong, D. Greig, H. E. Verdejo, M. Navarro, R. Lopez, B. Toro, C. Quiroga, G. Diaz-Araya, S. Lavandero and L. Garcia, *J. Card. Failure*, 2011, 17, 1012–1017.
  - 14 F. Fresquet, F. Pourageaud, V. Leblais, R. P. Brandes and J. P. Savineau, R. Marthan and B. Muller, *Br. J. Pharmacol.*, 2006, 148, 714–723.
  - 15 A. L. Firth, K. H. Yuill and S. V. Smirnov, *Am. J. Physiol.*, 2008, 295, L61–70.
  - 16 P. Seidel and M. Roth, *Mediators Inflammation*, 2013, 2013, 875403.
  - 17 S. Biswal, R. K. Thimmulappa and C. J. Harvey, *Proc. Am. Thorac. Soc.*, 2012, 9, 47–51.
  - 18 M. Meissner, E. M. Valesky, S. Kippenberger and R. Kaufmann, *J. Dtsch. Dermatol. Ges.*, 2012, 10, 793–801.
  - 19 C. M. Ha, S. Park, Y. K. Choi, J. Y. Jeong, C. J. Oh, K. H. Bae, S. J. Lee, J. H. Kim, K. G. Park, Y. Jun do and I. K. Lee, *Vasc. Pharmacol.*, 2014, 63, 29–36.
  - 20 C. J. Oh, J. Y. Kim, Y. K. Choi, H. J. Kim, J. Y. Jeong, K. H. Bae, K. G. Park and I. K. Lee, *PLoS One*, 2012, 7, e45870.
  - 21 L. Robles, N. D. Vaziri, S. Li, C. Takasu, Y. Masuda, K. Vo, S. H. Farzaneh, M. J. Stamos and H. Ichii, *Pancreas*, 2015, 44, 441–447.
  - 22 L. Robles, N. D. Vaziri, S. Li, Y. Masuda, C. Takasu, M. Takasu, K. Vo, S. H. Farzaneh, M. J. Stamos and H. Ichii, *PLoS One*, 2014, 9, e107111.
  - 23 R. Bompreszi, *Ther. Adv. Neurol. Disord.*, 2015, 8, 20–30.
  - 24 N. Lounsbury, G. Mateo, B. Jones, S. Papaiahgari, R. K. Thimmulappa, C. Teijaro, J. Gordon, K. Korzekwa, M. Ye, G. Allaway, M. Abou-Gharbia, S. Biswal and W. Childers, Jr., *Bioorg. Med. Chem.*, 2015, 23, 5352–5359.
  - 25 N. M. Reddy, H. R. Potteti, T. J. Mariani, S. Biswal and S. P. Reddy, *Am. J. Respir. Cell Mol. Biol.*, 2011, 45, 1161–1168.
  - 26 H. Wilms, J. Sievers, U. Rickert, M. Rostami-Yazdi, U. Mrowietz and R. Lucius, *J. Neuroinflammation*, 2010, 7, 30.
  - 27 P. Seidel, S. Goulet, K. Hostettler, M. Tamm and M. Roth, *Respir. Res.*, 2010, 11, 145.
  - 28 C. J. Harvey, R. K. Thimmulappa, S. Sethi, X. Kong, L. Yarmus, R. H. Brown, D. Feller-Kopman, R. Wise and S. Biswal, *Sci. Transl. Med.*, 2011, 3, 78ra32.
  - 29 X. L. Chen, S. E. Varner, A. S. Rao, J. Y. Grey, S. Thomas, C. K. Cook, M. A. Wasserman, R. M. Medford, A. K. Jaiswal and C. Kunsch, *J. Biol. Chem.*, 2003, 278, 703–711.
  - 30 T. Hosoya, A. Maruyama, M. I. Kang, Y. Kawatani, T. Shibata, K. Uchida, E. Warabi and N. Noguchi, K. Itoh and M. Yamamoto, *J. Biol. Chem.*, 2005, 280, 27244–27250.
  - 31 X. Cheng, R. C. Siow and G. E. Mann, *Antioxid. Redox Signaling*, 2011, 14, 469–487.
  - 32 S. C. Lo and M. Hannink, *Exp. Cell Res.*, 2008, 314, 1789–1803.
  - 33 S. Sharma, X. Sun, R. Rafikov, S. Kumar, Y. Hou, P. E. Oishi, S. A. Datar, G. Raff, J. R. Fineman and S. M. Black, *PLoS One*, 2012, 7, e41555.
  - 34 X. Sun, S. Kumar, S. Sharma, S. Aggarwal, Q. Lu, C. Gross, O. Rafikova, S. G. Lee, S. Dasarthy, Y. Hou, M. L. Meadows, W. Han, Y. Su, J. R. Fineman and S. M. Black, *Am. J. Respir. Cell Mol. Biol.*, 2014, 50, 1084–1095.
  - 35 X. Sun, S. Sharma, S. Fratz, S. Kumar, R. Rafikov, S. Aggarwal, O. Rafikova, Q. Lu, T. Burns, S. Dasarthy, J. Wright, C. Schreiber, M. Radman, J. R. Fineman and S. M. Black, *Antioxid. Redox Signaling*, 2013, 18, 1739–1752.
  - 36 M. C. Jaramillo and D. D. Zhang, *Genes Dev.*, 2013, 27, 2179–2191.
  - 37 J. Duan, F. G. Vogt, X. Li, D. Hayes, Jr. and H. M. Mansour, *Int. J. Nanomed.*, 2013, 8, 3489–3505.
  - 38 S. A. Meenach, K. W. Anderson, J. Zach Hilt, R. C. McGarry and H. M. Mansour, *Eur. J. Pharm. Sci.*, 2013, 49, 699–711.
  - 39 S. A. Meenach, F. G. Vogt, K. W. Anderson, J. Z. Hilt, R. C. McGarry and H. M. Mansour, *Int. J. Nanomed.*, 2013, 8, 275–293.
  - 40 L. Willis, D. Hayes, Jr. and H. M. Mansour, *Lung*, 2012, 190, 251–262.
  - 41 X. Wu, O. O. Adedoyin and H. M. Mansour, *Anti-Inflammatory Anti-Allergy Agents Med. Chem.*, 2011, 10, 215–229.
  - 42 J. Ahmad, S. Akhter, M. Rizwanullah, S. Amin, M. Rahman, M. Z. Ahmad, M. A. Rizvi, M. A. Kamal and F. J. Ahmad, *Nanotechnol., Sci. Appl.*, 2015, 8, 55–66.
  - 43 U. Ikoba, H. Peng, H. Li, C. Miller, C. Yu and Q. Wang, *Nanoscale*, 2015, 7, 4291–4305.
  - 44 F. Jia, X. Liu, L. Li, S. Mallapragada, B. Narasimhan and Q. Wang, *J. Controlled Release*, 2013, 172, 1020–1034.
  - 45 H. M. Mansour, Y. S. Rhee and X. Wu, *Int. J. Nanomed.*, 2009, 4, 299–319.



- 46 X. Li, F. G. Vogt, D. Hayes, Jr. and H. M. Mansour, *J. Aerosol Med. Pulm. Drug Delivery*, 2014, 27, 81–93.
- 47 X. Li, F. G. Vogt, D. Hayes, Jr. and H. M. Mansour, *J. Pharm. Sci.*, 2014, 103, 2937–2949.
- 48 S. A. Meenach, K. W. Anderson, J. Z. Hilt, R. C. McGarry and H. M. Mansour, *AAPS PharmSciTech*, 2014, 15, 1574–1587.
- 49 S. Lopes, L. Lapinski and R. Fausto, *Phys. Chem. Chem. Phys.*, 2002, 4, 3965–3974.
- 50 P. Muralidharan, M. Malapit, E. Mallory, D. Hayes, Jr. and H. M. Mansour, *Nanomedicine*, 2015, 11, 1189–1199.
- 51 X. Li and H. M. Mansour, *AAPS PharmSciTech*, 2011, 12, 1420–1430.
- 52 X. Li, F. G. Vogt, D. Hayes, Jr. and H. M. Mansour, *Eur. J. Pharm. Sci.*, 2014, 52, 191–205.
- 53 C. W. Park, X. Li, F. G. Vogt, D. Hayes, Jr., J. B. Zwischenberger, E. S. Park and H. M. Mansour, *Int. J. Pharm.*, 2013, 455, 374–392.
- 54 N. A. Stocke, S. A. Meenach, S. M. Arnold, H. M. Mansour and J. Z. Hilt, *Int. J. Pharm.*, 2015, 479, 320–328.
- 55 X. Wu, D. Hayes, Jr., J. B. Zwischenberger, R. J. Kuhn and H. M. Mansour, *Drug Des., Dev. Ther.*, 2013, 7, 59–72.
- 56 R. Vehring, *Pharm. Res.*, 2008, 25, 999–1022.
- 57 S. Suarez and A. J. Hickey, *Respir. Care*, 2000, 45, 652–666.
- 58 K. Aoshiba and A. Nagai, *Clin. Rev. Allergy Immunol.*, 2004, 27, 35–43.

